J|A|C|S
ARTICLES
Published on Web 12/09/2006

Seeded Growth of Asymmetric Binary Nanocrystals Made of a Semiconductor TiO_2 Rodlike Section and a Magnetic γ-Fe_2O_3 Spherical Domain

Raffaella Buonsanti,[†] Vincenzo Grillo,[‡] Elvio Carlino,[‡] Cinzia Giannini,[§] Maria Lucia Curri,[||] Claudia Innocenti,[⊥] Claudio Sangregorio,[⊥] Klaus Achterhold,[#] Fritz Günter Parak,[#] Angela Agostiano,[†,||] and Pantaleo Davide Cozzoli*[,†,▽]

Contribution from the Dipartimento di Chimica, Università di Bari, via Orabona 4, I-70126 Bari, Italy, TASC-INFM-CNR National Laboratory, Area Science Park - Basovizza, Building MM, SS 14, Km 163.5, I-34012 Trieste, Italy, CNR-Istituto di Cristallografia (IC), via Amendola 122/O, I-70126 Bari, Italy, CNR-Istituto per i Processi Chimico-Fisici (IPCF), sez. Bari, via Orabona 4, I-70126 Bari, Italy, LA.M.M. UdR INSTM, Dipartimento di Chimica, Università di Firenze, Via della Lastruccia 3, I-50019 Sesto Fiorentino, Italy, Physik-Department E17, Technische Universität München, James-Franck-Strasse, D-85747 Garching, Germany, National Nanotechnology Laboratory of CNR-INFM, Unità di Ricerca IIT, Distretto Tecnologico ISUFI, via per Arnesano km 5, I-73100 Lecce, Italy

Received September 11, 2006; E-mail: davide.cozzoli@unile.it

Abstract: Asymmetric binary nanocrystals (BNCs), comprising one *c*-axis elongated anatase TiO_2 section and one γ-Fe_2O_3 spherical domain attached together, are synthesized by heterogeneous nucleation of iron oxide onto the longitudinal facets of TiO_2 nanorods in a ternary surfactant mixture. The topologically controlled composition of the BNCs is ascertained by a combination of powder X-ray diffraction, Raman and Mössbauer spectroscopy, high-angle annular dark-field imaging, and high-resolution transmission electron microscopy lattice fringe mapping, while their size-dependent magnetic behavior is demonstrated by ac susceptibility measurements. The heteroepitaxial growth proceeds through a mechanism never observed before for colloidal nanoheterostructures: the two domains share a restricted and locally curved junction region, which accommodates efficiently the interfacial strain and retards the formation of misfit dislocations. It is believed that these BNCs, which combine the properties of two technologically relevant oxide materials, can pave the way to reinforced applications in several fields of nanoscience, such as in photocatalysis, in malignant cell treatments, and in nanocrystal assembly.

1. Introduction

In the last years, advances in colloidal chemistry approaches have opened up access to a variety of size- and shape-tailored inorganic nanocrystals (NCs), enabling verification of dimensionality-dependent chemical-physical laws of nanoscale matter.[1,2] Owing to their robustness and processability, NCs are being currently integrated with existing devices and exploited in the bottom-up fabrication of innovative materials.[3−5] Although refinement in the dimensional and morphological regimes of nanoparticles is still desirable, a further step toward structural complexity and increased functionality has been recently devised with the synthesis of hybrid NCs with a topologically controlled composition, i.e., consisting of two or more chemically different material sections grouped together through an inorganic junction.[6−21] As a result of the combination of the properties that distinguish each crystalline domain, such composite particles hold promise as first prototypes of "smart" NCs, i.e., nanosized objects potentially able to perform multiple tasks, such as in

[†] Università di Bari.
[‡] TASC-INFM-CNR National Laboratory.
[§] CNR-Istituto di Cristallografia (IC).
[||] CNR-Istituto per i Processi Chimico-Fisici (IPCF).
[⊥] Università di Firenze.
[#] Technische Universität München.
[▽] National Nanotechnology Laboratory of CNR-INFM.

(1) (a) Burda, C.; Chen, X.; Narayanan, R.; El-Sayed, M. A. *Chem. Rev.* **2005**, *105*, 1025. (b) Jun, Y.-w.; Choi, J.-s.; Cheon, J. *Angew. Chem., Int. Ed.* **2006**, *45*, 3414.
(2) (a) Lisiecki, I. *J. Phys. Chem. B* **2005**, *109*, 12231. (b) Murphy, C. J.; Sau, T. K.; Gole, A. M.; Orendorff, C. J.; Gao, J.; Gou, L.; Hunyadi, S. E.; Li, T. *J. Phys. Chem. B* **2005**, *109*, 13857.
(3) (a) Shipway, A. N.; Katz, E.; Willner, I. *ChemPhysChem.* **2000**, *1*, 18. (b) Huynh, W. U.; Dittmer, J.; Alivisatos, A. P. *Science* **2002**, *295*, 2425. (c) Narayanan, R.; El-Sayed, M. A. *J. Phys. Chem. B* **2005**, *109*, 12663.
(4) (a) Rosi, N. L.; Mirkin, C. A. *Chem. Rev.* **2005**, *105*, 1547. (b) Bakalova, R.; Ohba, H.; Zhelev, Z.; Ishikawa, M.; Baba, Y. *Nat. Biotechnol.* **2004**, *22*, 1360.
(5) (a) Cozzoli, P. D.; Manna, L. *Nat. Mater.* **2005**, *4*, 801. (b) Pellegrino, T.; Kudera, S.; Liedl, T.; Munoz Javier, A.; Manna, L.; Parak, W. J. *Small* **2005**, *1*, 48. (c) Love, J. C.; Estroff, L. A.; Kriebel, J. K.; Nuzzo, R. G.; Whitesides, G. M.; Love, J. C. *Chem. Rev.* **2005**, *105*, 1103.
(6) Cozzoli, P. D.; Pellegrino, T.; Manna, L. *Chem. Soc. Rev.* **2006**, *35*, 1195.
(7) (a) Srnova-Sloufova, I.; Vlckova, B.; Bastl, Z.; Hasslett, T. L. *Langmuir* **2004**, *20*, 3407. (b) Rodriguez-Gonzalez, B.; Burrows, A.; Watanabe, M.; Kiely, C.; Liz-Marzan, L. M. *J. Mater. Chem.* **2005**, *15*, 1755. (c) Yang, J.; Lee, J. Y.; Too, H.-P. *J. Phys. Chem. B* **2005**, *109*, 19208.
(8) (a) Li, J. J.; Wang, A. Y.; Guo, W.; Keay, J. C.; Mishima, T. D.; Johnson, M. B.; Peng, X. *J. Am. Chem. Soc.* **2003**, *125*, 12567. (b) Talapin, D.V.; Mekis, I.; Gotzinger, S.; Kornowski, A.; Benson, O.; Weller, H. *J. Phys. Chem. B* **2004**, *108*, 18826. (c) Kim, S.; Fisher, B.; Eisler, H. J.; Bawendi, M. *J. Am. Chem. Soc.* **2003**, *125*, 11466. (d) Yu, K.; Zaman, B.; Romanova, S.; Wang, D-s.; Ripmeester, J. A. *Small* **2005**, *1*, 332.

biomedical engineering, diagnostics, sensing, and catalysis.[5] Therefore, the development of multifunctional nanocrystal heterostructures appears to be the natural direction toward which wet-chemistry research will have to increasingly orient.

In colloidal media, the size and shape evolution of NCs is driven by both thermodynamic parameters (e.g., relative stability of crystal polymorphs) and kinetically limited growth processes (e.g., diffusion of reactants, surface adhesion of surfactants).[1−2] However, when attempting to assemble different materials together at the nanoscale, crystal miscibility, interfacial strain, and face-selective reactivity come also into play.[6] Judicious adjustment of the chemical environment critically affects these parameters, dictating the growth mode of the resulting architecture.[6−21]

A large interface can be shared between two materials if the respective lattice constants do not differ significantly and/or if the interfacial energy is kept low during the synthesis. These conditions lead to the formation of core/shell type NCs, in which the symmetry of the starting core is usually retained following coverage by a different inorganic layer.[7−12] Associations of various semiconductors, metals and oxides in onionlike configurations often exhibit distinct properties as compared to those inherent to the individual components, such as enhanced or tunable plasmon absorption[7] or photoluminescence,[8] modified magnetic behavior,[9−10] and improved photocatalytic and photoelectrochemical responses,[11−12] depending on the specific combination.

In the case of materials that possess limited miscibility or large interfacial energy, or when a starting NC exhibits remarkable facet-dependent chemical reactivity, more elaborate architectures are likely to form, which can comprise two or more nearly discrete inorganic domains epitaxially connected via a small junction area.[13−21] For instance, phase-segregated Co−Pd sulfide and Cu−In sulfide NC heterostructures sharing an interface of graded composition have been prepared by co-reacting the respective molecular precursors, during which the selective nucleation of the one material is followed by overgrowth of the other one.[13] Several types of nanocrystal hetero-oligomers have been synthesized by various seed-mediated mechanisms. FePt−CdS and γ-Fe_2O_3−MeS (where Me═Zn, Cd, Hg) dimers have been obtained by a thermally activated coalescence of an initially deposited amorphous metal sulfide shell into a separate grain attached at one side of the starting seed.[14] Facet-preferential deposition of a second material onto preformed particles has been largely exploited to achieve binary heterostructures, such as of Au−Fe_3O_4,[15] FePt−Ag, Fe_3O_4−Ag,[16] Ag−Se,[17] $CoPt_3$−Au,[18a] and PbS−Au.[18b] This strategy has been further implemented to produce ternary NCs by nucleating an additional domain on dimer seeds or by making binary NCs react with each other.[19] On anisotropically shaped NCs, such as wurtzite nanorods and tetrapods, it has been possible to grow a different inorganic domain exclusively at certain locations of the starting particles, which correspond to the facets with the highest reactivity.[20−23] Remarkable demonstrations of this concept are illustrated by the preparation of CdS−CdSe−CdTe heterostructures with linear or branched topology,[20] CdSe or CdS nanorods decorated with either a single or two Au,[21a,b] CdTe,[21c] or PbSe tips,[22] and ZnO nanorods with site-specific Ag deposits.[23]

Noncentrosymmetric hybrid NCs with discrete inorganic sections could considerably extend the technological performances of the individual components. For instance, the properties inherent to each NC domain, such as magnetism, optical absorption, or fluorescence, are naturally modified as a result of the contact junction with another material.[15,18,19,22] In semiconductor heterostructures, depending on the relative band gap alignment of the components, the charge carriers can be either localized preferentially in one domain[22] or separated more efficiently,[18b,20] which could have important implications in optoelectronic and photovoltaic applications. Also, hybrid NCs have allowed the introduction of anisotropic distributions of surface functional groups, facilitating the site-specific anchoring of biomolecules[16] or the controlled assembly of NCs.[5a,21a] Exciting technological perspectives are thus emerging, which fully justify further efforts toward the realization of novel types of hybrid NCs.

The present work makes an advance in this field, as it reports on the synthesis of colloidal nanoheterostructures based on TiO_2 and γ-Fe_2O_3 (maghemite), which so far have been tentatively combined in the core−shell configuration only.[24] TiO_2 is the most studied semiconductor oxide, owing to its widespread applications in light-assisted environmental cleanup,[25] in solar energy conversion,[26] in sensing,[27] and, more recently, in the

(9) (a) Mandal, M.; Kundu, S.; Ghosh, S. K.; Panigrahi, S.; Sau, T. K.; Yusuff, S. M.; Pal, T. *J. Colloid Interface Sci.* **2005**, *286*, 187. (b) Wang, L. Y.; Luo, J.; Fan, Q.; Suzuki, M.; Suzuki, I. S.; Engelhard, M. H.; Lin, Y.; Kim, N.; Wang, J. Q.; Zhong, C. J. *J. Phys. Chem. B* **2005**, *109*, 21593. (c) Wang, H.; Brandl, D. W.; Le, F.; Nordlander, P.; Halas, N. J. *Nano Lett.* **2006**, *6*, 827.

(10) (a) Zeng, H.; Li, J.; Wang, Z. L.; Liu, J. P.; Sun, S. H. *Nano Lett.* **2004**, *4*, 187. (b) Kim, H.; Achermann, M.; Balet, L. P.; Hollingsworth, J. A.; Klimov, V. I. *J. Am. Chem. Soc.* **2005**, *127*, 544. (c) Park, J.; Kim, M. J.; Jun, Y.-w; Lee, J. S.; Lee, W.-R.; Cheon, J. **2004**, *126*, 9073. (d) Ban, Z.; Barnokov, Y. A.; Li, F.; Golub, V. O.; O'Connor, C. J. *J. Mater. Chem.* **2005**, *15*, 4660. (e) Lu, Z.; Prouty, M. D.; Guo, Z.; Golub, V. O.; Kumar, C. S. S. R.; Lvov, Y. M. *Langmuir* **2005**, *21*, 2042.

(11) (a) Subramanian, V.; Wolf, E.; Kamat, P. V. *Langmuir* **2003**, *19*, 469. (b) Subramanian, V; Wolf, E. E.; Kamat, P. V. *J. Phys. Chem. B* **2003**, *107*, 7479. (c) Hirakawa, T.; Kamat, P. V. *J. Am. Chem. Soc.* **2005**, *127*, 3928.

(12) (a) Liz-Marzan, L. M.; Mulvaney, P. *J. Phys. Chem. B* **2003**, *107*, 7312. (b) Guo, Y. G.; Wan, L.-J.; Bai, C. L. *J. Phys. Chem. B* **2003**, *107*, 5441. (c) Li, J.; Zeng, H. C. *Angew. Chem.* **2005**, *117*, 4416.

(13) (a) Teranishi, T.; Inoue, Y.; Nakaya, M.; Oumi, Y.; Sano, T. *J. Am. Chem. Soc.* **2004**, *126*, 9914. (b) Choi, S.-H.; Kim, E.-G.; Hyeon, T. *J. Am. Chem. Soc.* **2006**, *128*, 2520.

(14) (a) Gu, H.; Zheng, R.; Zhang, X.; Xu, B. *J. Am. Chem. Soc.* **2004**, *126*, 5664. (b) Kwon, K.-W.; Shim, M. *J. Am. Chem. Soc.* **2005**, *127*, 10269.

(15) Yu, H.; Chen, M.; Rice, P. M.; Wang, S. X.; White, R. L.; Sun, S. *Nano Lett.* **2005**, *5*, 379.

(16) Gu, H.; Yang, Z.; Gao, J.; Chang, C. K.; Xu, B. *J. Am. Chem. Soc.* **2005**, *127*, 34.

(17) Gao, X.; Yu, L.; MacCuspie, R. I.; Matsui, H. *Adv. Mater.* **2005**, *17*, 426.

(18) (a) Pellegrino, T.; Fiore, A.; Carlino, E.; Giannini, C.; Cozzoli, P. D.; Ciccarella, G.; Respaud, M.; Palmirotta, L.; Cingolani, R.; Manna, L. *J. Am. Chem. Soc.* **2006**, *128*, 6690. (b) Yang, J.; Elim, I. H.; Zhang, Q. B.; Lee, J. Y.; Ji, W. *J. Am. Chem. Soc.* **2006**, *128*, 11921.

(19) (a) Shi, W.; Zeng, H.; Sahoo, Y.; Ohulchanskyy, T. Y.; Ding, Y.; Wang, Z. L.; Prasad, P. N. *Nano Lett.* **2006**, *6*, 875. (b) Shi, W.; Sahoo, Y.; Zeng, H.; Ding, Y.; Swihart, M. T.; Prasad, P. N. *Adv. Mater.* **2006**, *18*, 1899.

(20) (a) Milliron, D. J.; Hughes, S. M.; Cui, Y.; Manna, L.; Li, J.; Wang, L.-W.; Alivisatos, A. P. *Nature* **2004**, *430*, 190. (b) Shieh, F.; Saunders, A. E.; Korgel, B. A. *J. Phys. Chem. B* **2005**, *109*, 8538.

(21) (a) Molari, T.; Rothenberg, E.; Popov, I.; Costi, R.; Banin, U. *Science* **2004**, *304*, 1787. (b) Mokari, T.; Sztrum, C. G.; Salant, A.; Rabani, E.; Banin, U. *Nat. Mater.* **2005**, *4*, 855. (c) Carbone, L.; Kudera, S.; Giannini, C.; Ciccarella, G.; Cingolani, R.; Cozzoli, P. D.; Manna, L. *J. Mater. Chem.* **2006**, *16*, 3952.

(22) Kudera, S.; Carbone, L.; Casula, M. F.; Cingolani, R.; Falqui, A.; Snoeck, E.; Parak, W. J.; Manna, L. *Nano Lett.* **2005**, *5*, 445.

(23) Pacholski, C.; Kornowski, A.; Weller, H. *Angew. Chem., Int. Ed.* **2004**, *43*, 4774.

(24) (a) Beydoun, D.; Amal, R.; Low, G. K.-C.; McEvoy, S. *J. Phys. Chem. B* **2000**, *104*, 4387. (b) Chen, F.; Xie, Y.; Zhao, J.; Lu, G. *Chemosphere* **2001**, *44*, 1159. (c) Chen, C.-T.; Chen, Y.-C. *Anal. Chem.* **2005**, *77*, 5912. (d) Gao, Y.; Chen, B.; Li, H.; Ma, Y. *Mater. Chem. Phys.* **2003**, *80*, 348.

(25) (a) Beydoun, D.; Amal, R.; Low, G.; McEvoy, S. *J. Nanopart. Res.* **1999**, *1*, 439. (b) Konstantinou, I. K.; Albanis, T. A. *Appl. Catal., B* **2004**, *49*, 1. (c) Comparelli, R.; Fanizza, E.; Curri, M. L.; Cozzoli, P. D.; Mascolo, M.; Passino, R.; Agostiano, A. *Appl. Catal., B* **2005**, *55*, 81.

photodeactivation of microorganisms[28a−c] and of malignant cells.[28d−h] Nanosized iron oxide possesses attractive catalytic activity,[29] remarkable size- and shape-dependent magnetic properties,[30] and promising applications in sensing,[31] biomedical diagnostics,[32a−c] and cancer treatment.[32d−i]

We report a straightforward colloidal approach to fabricate a new type of highly asymmetric binary nanocrystal (BNC), made of one spherical γ-Fe_2O_3 particle epitaxially grown on a lateral facet of a rodlike anatase TiO_2 domain. The BNCs were obtained by selective heterogeneous nucleation of iron oxide onto *c*-axis-elongated TiO_2 nanorods in the presence of oleic acid, oleyl amine, and dodecan-1,2-diol at high temperature. The chemical and structural identity of each heterostructure domain was ascertained by a combination of powder X-ray Diffraction, Raman and Mössbauer spectroscopy, high-angle annular dark-field (HAADF) imaging, and high-resolution transmission electron microscopy (HRTEM) analyses. The BNCs exhibit the characteristic size-dependent magnetic behavior of maghemite, as indicated by ac susceptibility measurements. A striking structural feature of the BNCs is that the nanorod section is slightly bowed in proximity of the γ-Fe_2O_3 sphere, and follows its curvature at the junction region. Detailed lattice fringe mapping actually revealed that the coherent attachment between γ-Fe_2O_3 and TiO_2 lattices proceeds similarly to one of the known mechanisms leading to the low defect density growth of quantum dot islands onto highly mismatched substrates by epitaxial growth techniques, like molecular beam epitaxy: i.e., the two domains share a rather restricted interface that is locally bent to decrease the interfacial strain (mostly due to the large misfit between the two lattices) retarding the formation of dislocations. To the best of our knowledge, it is the first time that such a mechanism of heteroepitaxial growth is observed for colloidal hybrid nanostructures. Finally, we will also briefly outline the technological potential of such combined semiconductor/magnetic nanocrystals in several fields of nanoscience.

2. Experimental Section

2.1 Materials. All chemicals were of the highest purity available and were used as received without further purification. Titanium tetraisopropoxide ($Ti(OPr^i)_4$ or TTIP, 97%), titanium tetrachloride ($TiCl_4$, 99.999%), trimethylamine *N*-oxide dihydrate ($(CH_3)_3NO{\cdot}2H_2O$ or TMAO, 98%), oleic acid ($C_{17}H_{33}CO_2H$ or OLAC, 90%), 1-octadecene ($C_{18}H_{36}$ or ODE, 90%), oleyl amine ($C_{17}H_{33}NH_2$ or OLAM, 70%), iron pentacarbonyl ($Fe(CO)_5$, 98%), and dodecan-1,2-diol ($C_{12}H_{24}(OH)_2$ or DDIOL, 90%) were purchased from Aldrich. All solvents used were of analytical grade and purchased from Aldrich. Reference materials for Mössbauer measurements, namely bulk magnetite (Fe_3O_4, 98%), bulk maghemite (γ-Fe_2O_3, 99%), and bulk hematite (α-Fe_2O_3, 99.99%) were purchased from Sigma-Aldrich, Alpha Aesar Johnson Mattey Company, and Chem-Pur, respectively.

2.2 Synthesis of TiO_2/γ-Fe_2O_3 Binary Nanocrystals (BNCs). Unless otherwise stated, all syntheses were carried out under air-free conditions using the standard Schlenk line setup.

Synthesis of TiO_2 Nanorods. Organic-capped anatase TiO_2 nanorods (NRs) with different geometric parameters were synthesized by slightly modified literature protocols.[33] TiO_2 NRs with an average diameter of ∼3−4 nm and a mean length of ∼25−30 nm were obtained by low-temperature TMAO-catalyzed hydrolysis of TTIP.[33a] In a typical synthesis, 15 mmol of TTIP was dissolved in 70 g of degassed OLAC, and the resulting solution was then reacted with 5 mL of an aqueous 2 M TMAO solution at 100 °C for 48 h. Larger TiO_2 NRs, i.e., with an average diameter of ∼5−7 nm and a mean length of ∼50−70 nm, were synthesized by thermal decomposition of titanium−oleate complexes.[33b] In a typical preparation, 6 g of ODE, 26 mmol of OLAM, and 2 mmol of OLAC were carefully degassed at 120 °C for 20 min, after which the mixture was put under N_2 flow. Then, 2 mmol of $TiCl_4$ were added at 40 °C, and the flask was heated to 280 °C for 30 min.

The TiO_2 NRs were separated from their growing mixture upon ethanol addition and subsequently subjected to repeated cycles of redissolution in $CHCl_3$ and precipitation with acetone to wash out surfactant residuals. Finally, an optically clear 1 M TiO_2 stock solution in $CHCl_3$ was prepared for the synthesis of the heterostructures. The TiO_2 concentration was expressed with reference to its TTIP precursor, which was assumed to be converted completely into TiO_2 during the NR synthesis.

Synthesis of BNCs. As a general procedure, calibrated amounts of the TiO_2 stock solution (corresponding to 0.1−3 mmol of TiO_2), of DDIOL, OLAM, OLAC, and 20 mL of ODE were loaded together in a 100-mL three-neck flask connected to a reflux condenser. The mixture was pumped to vacuum for 20 min at 120 °C, after which it was heated up under N_2 flux to the temperature selected for the iron precursor injection (ranging from to 240 °C to 300 °C). Then, 1 mL of a $Fe(CO)_5$ solution (typically 0.1−2 M) in previously degassed ODE was added in a single portion (in less than 0.1 s) to the vigorously stirred mixture. In all the syntheses, the $Fe(CO)_5$/OLAC/OLAM/DDIOL molar ratio was set at 1:3:1.5:2.5 (as determined empirically by a number of preliminary experiments), while the $Fe(CO)_5/TiO_2$ molar ratio ranged from 1:1 to 10:1. Whenever desired, multiple $Fe(CO)_5$ injections could also be performed to enlarge the size of the iron oxide particles. The

(26) (a) Bignozzi, C. A.; Argazzi, R.; Kleverlaan, C. J. *Chem. Soc. Rev.* **2000**, *29*, 87. (b) Hagfeldt, A.; Gratzel, M. *Acc. Chem. Res.* **2000**, *33*, 269. (c) Nelson, J. *Curr. Opin. Solid State Mater. Sci.* **2002**, *6*, 87.

(27) (a) Grubert, G.; Stockenhuber, M.; Tkachenko, O. P.; Wark, M. *Chem. Mater.* **2002**, *14*, 2458. (b) Zhu, Y.; Shi, J.; Zhang, Z.; Zhang, C.; Zhang, X. *Anal. Chem.* **2002**, *74*, 120. (c) Manera, M. G.; Leo, G.; Curri, M. L.; Cozzoli, P. D.; Rella, R.; Siciliano, P.; Agostiano, A.; Vasanelli, L. *Sens. Actuators, B* **2004**, *100*, 75.

(28) (a) Fu, G.; Vary, P. S.; Lin, C.-T. *J. Phys. Chem B* **2005**, *109*, 8889. (b) Han, S.; Choi, S.-H.; Kim, S.-S.; Cho, M.; Jang, B.; Kim, D.-Y.; Yoon, J.; Hyeon, T. *Small* **2005**, *1*, 812. (c) Huang, N. P.; Xiao, Z.D.; Huang, D.; Yuan, C.W. *Supramol. Sci.* **1998**, *5*, 559. (d) Cai, R.; Hashimoto, K.; Itoh, K.; Kubota, Y.; Fujishima, A. *Bull. Chem. Soc. Jpn.* **1991**, *64*, 1268. (e) Linnainmaa, K.; Kivipensas, P.; Vainio, H. *Toxicol. in Vitro* **1997**, *11*, 329. (f) Xu, M.; Ma, J.; Gu, Y.; Lu, Z. *Supramol. Sci.* **1998**, *5*, 511. (g) Xu, M.; Huang, N.; Xiao, Z.; Lu, Z. *Supramol. Sci.* **1998**, *5*, 449. (h) Uchino, T.; Tokunaga, H.; Ando, M.; Utsumi, H. *Toxicol. In Vitro* **2002**, *16*, 629.

(29) (a) Miser, D. E.; Shin, E. J.; Hajaligol, M. R.; Rasouli, F. *Appl. Catal., A* **2004**, *258*, 7. (b) Bedford, R. B.; Betham, M.; Bruce, D. W.; Davis, S.A.; Frost, R. M.; Hird, M. *Chem. Commun.* **2006**, 1398. (c) Shin, E. J; Miser, D. E.; Chan, W. G.; Hajaligol, M. R. *Appl. Catal., B* **2005**, *61*, 79. (d) Moura, F. C. C.; Oliveira, G. C.; Araujo, M. H.; Ardisson, J. D.; Macedo, W. A.A.; Lago, R. M. *Appl. Catal., A* **2006**, *307*, 195.

(30) (a) Hyeon, T.; Lee, S. S.; Park, J.; Chung, Y.; Na, H. B. *J. Am. Chem. Soc.* **2001**, *123*, 12798. (b) Park, J.; An, K.; Hwang, Y.; Park, J.-G.; Noh, H.-J.; Kim, J.-Y.; Park, J.-H.; Hwang, N.-M.; Hyeon, T. *Nat. Mater.* **2004**, *3*, 891. (c) Park, J.; Lee, E.; Hwang, N.-M.; Kang, M.; Kim, S. C.; Hwang, Y.; Park, J.-G.; Noh, H.-J.; Kim, J.-Y.; Park, J.-H; Hyeon, T. *Angew. Chem., Int. Ed.* **2005**, *44*, 2872. (d) Woo, K.; Hong, J.; Choi, S.; Lee, H.-W.; Ahn, J.-P.; Kim, C. S.; Lee, S. W. *Chem. Mater.* **2004**, *16*, 2814. (e) Lee, Y.; Lee, J.; Bae, C. J.; Park, J.-G.; Noh, H.-J.; Park, H.-J.; Hyeon, T. *Adv. Funct. Mater.* **2005**, *15*, 503.

(31) (a) Katz, E.; Willner, I. *Chem. Commun.* **2005**, 4089. (b) Kim, K. S.; Park, J.-K. *Lab Chip* **2005**, *6*, 657.

(32) (a) Huh, Y.-M-; Jun, Y.-w; Song, H.-T.; Kim, S.; Choi, J.-s.; Lee, J.-H.; Yoon, S.; Kim, K.-S.; Shin, J.-S.; Suh, J.-S.; Cheon, J. *J. Am. Chem. Soc.* **2005**, *127*, 12387. (b) Song, H.-T.; Choi, J.-s.; Huh, Y.-M.; Kim, S.; Jun, Y.-w.; Suh, J.-S.; Cheon, J. *J. Am. Chem. Soc.* **2005**, *127*, 9992. (c) Jun, Y.-w.; Huh, Y.-M.; Choi, J.-s.; Lee, J.-H.; Song, H.-T.; Kim, S.-j.; Yoon, S.; Kim, K.-S.; Shin, J.-S.; Suh, J.-S.; Cheon, J. *J. Am. Chem. Soc.* **2005**, *127*, 5732. (d) Jordan, A.; Scholz, R.; Maier-Hauff, K.; Johannesen, M.; Wust, P.; Nadobny, J.; Schirra, H.; Schmidt, H.; Deger, S.; Loening, S.; Lanksch, W.; Felix, R. *J. Magn. Magn. Mater.* **2001**, *225*, 118. (e) Hergt, R.; Hiergeist, R.; Hilger, I.; Kaiser, W. A.; Lapatnikov, Y.; Margel, S.; Richter, U. *J. Magn. Magn. Mater.* **2004**, *270*, 345. (f) Hilger, I.; Hergt, R.; Kaiser, W. A. *J. Magn. Magn. Mater.* **2005**, *293*, 314. (g) Wang, X.; Gu, H.; Yang, Z. *Magn. Magn. Mater.* **2005**, *293*, 334. (h) Gonzales, M.; Krishnan, K. M. *J. Magn. Magn. Mater.* **2005**, *293*, 265. (i) Park, S. I.; Hwang, Y. H.; Lim, J. H.; Kim, J. H.; Yun, H. I.; Kim, C. O. *J. Magn. Magn. Mater.* **2006**, *304*, e403.

(33) (a) Cozzoli, P. D.; Kornowski, A.; Weller, H. *J. Am. Chem. Soc.* **2003**, *125*, 14539. (b) Seo, J.-w.; Jun, Y.-w.; Ko, S. J.; Cheon, J. *J. Phys. Chem. B* **2005**, *109*, 5389.

fast precursor injection caused a sudden drop of ~20−40 °C, after which the temperature was allowed to slowly recover to the initial value. Release of white vapors was also observed soon after $Fe(CO)_5$ addition and the solution turned from yellowish to light brown to black over a period of 1−10 min, depending on the $Fe(CO)_5$ concentration. Note that no relevant color change was detected for syntheses carried out at temperatures lower than ~220 °C, and no iron oxide product could be finally recovered even after reaction times as long as 24 h. The growth of iron oxide was accomplished under N_2 for a total period of 1 h, after which the mixture was allowed to cool down to 120 °C. At this point, the flask was exposed to air and kept at this temperature for 1 h. Under these conditions, the decomposition of reactive species, and hence additional growth of iron oxide, was inhibited, and only further oxidation of the initially formed product could occur.

Monitoring Nanocrystal Growth. The temporal evolution of BNC growth was monitored by extracting aliquots of the hot reaction mixture via a glass syringe at scheduled time intervals. The aliquots were suddenly cooled down to 120 °C and exposed to air for 1 h.

Extraction Procedures. After the synthesis, the extraction/purification procedures of the BNCs were carried out under ambient atmosphere. 2-propanol was added to the reaction mixture at room temperature, and the solution was centrifuged at 3000 rpm for 30 min. The precipitate was washed twice with acetone to remove precursor and surfactant residuals. Finally, the BNC product could be fully redissolved in nonpolar solvents, such as toluene, chloroform, and hexane. Whenever necessary, size-selective precipitation by repeated cycles of calibrated alcohol addition and centrifugation was applied to enrich the samples with BNCs, while unreacted TiO_2 NRs and iron oxide NCs that had nucleated separately remained dissolved in the supernatant.

2.3 Characterization of the Heterostructures. Transmission Electron Microscopy (TEM). Low-resolution TEM images were recorded with a Jeol Jem 1011 microscope operating at an accelerating voltage of 100 kV. Phase contrast high-resolution transmission electron microscopy (HRTEM) and high-angle annular dark-field scanning transmission electron microscopy (HAADF-STEM) experiments were performed by using a Jeol 2010F TEM/STEM microscope equipped with YAP large-angle detector for HAADF imaging. The microscope was operated at 200 keV, corresponding to an electron wavelength of 0.00251 nm. The objective lens had a spherical aberration coefficient of 0.47 ± 0.01 nm and hence a resolution at optimum defocus of 0.19 nm in HRTEM[34] and of 0.126 nm in HAADF imaging.[35] TEM samples were prepared by dropping a dilute solution of the NCs in toluene on carbon-coated copper grids and then allowing the solvent to evaporate.

The spatial distribution of the two lattices in the BNCs was mapped by analyzing the local amplitude of the periodicity characteristic of each phase. To obtain the amplitude as a point-to-point information, the Fourier transform of the image was considered according to Hÿtch et al.[36] The contribution to the image, arising from each Fourier peak can be written as:

$$I(\bar{r}) \approx H_g(\bar{r}) \exp(i2\pi\bar{g}\cdot\bar{r}) \quad (1)$$

where $I(\bar{r})$ is the image intensity at the position vector $\bar{r}$, $\bar{g}$ is the reciprocal lattice vector, and the factor $H_g(\bar{r})$ represents the local value of the Fourier coefficient of the fringes. To extract $H_g(\bar{r})$, the selected Fourier peak was isolated by multiplying it with a Gaussian mask, $M(\bar{k})$:[36]

$$M(\bar{k}) = \exp\left(-\frac{(\bar{k}-\bar{g})^2}{\sigma^2}\right) \quad (2)$$

(where σ is the width of the mask and $\bar{k}$ is the wave vector) in order to exclude other periodicities (σ was chosen of the order of 5 nm^{-1}). The as-derived Fourier spectrum was then back transformed and the resulting image multiplied by $\exp(-i2\pi\bar{g}\,\bar{r})$ to remove the exponential factor. The amplitude of $H_g(\bar{r})$ was then derived to construct a map of the local amplitude of the fringes. The maps obtained by this method were superimposed using a different color for each phase. The spatial resolution of this techniques is determined by the size of the Gaussian mask that imposes a limited bandwidth to the resulting map.

Statistics. A statistical analysis was carried out on several wide-field, low-magnification TEM images, with the help of a dedicated software (Axio Vision). For each sample, at least 500 particles were counted. To measure the length of the NR sections, we considered those BNCs that were oriented on the grid such that the plane intersecting both domains was perpendicular to the electron beam. For these BNCs, the rodlike TiO_2 domain could therefore be observed entirely, along with the iron oxide sphere attached laterally. The diameter of the NRs as well as the size of the spherical NCs was accurately measurable regardless of the orientation of the BNCs. For the purpose of the following discussion,

$$\text{heterostructure yield} = \frac{100 \times \text{the number of BNCs}}{\text{the number of isolated NRs} + \text{the number of BNCs}}$$

Power X-ray Diffraction (XRD). XRD measurements were performed with a NONIUS KappaCCD single-crystal diffractometer equipped with a 3 kW generator molybdenum tube, with a high-precision four-circle goniometer, and with a low noise and high sensitivity CCD detector. The samples were measured in Debye−Scherrer configuration using Lindemann capillaries (0.5-mm diameter) that were filled with dried NC powder. The images were folded into powder diffraction patterns using the FIT2D software[37a] after calibrating the detector with Si-NIST (640c) powder standard. Due to the instrumental resolution function, crystalline domains larger than ~4 nm could not be discriminated by their XRD peak broadening.

Quantitative phase analysis (QPA) was performed with a whole profile pattern fitting (WPPF) method which can be safely applied to mixtures of crystallographic phases, provided that the average crystalline domain size is about 10 times the unit cell.[37b] The BNC samples were described as mixtures of TiO_2 anatase and spinel cubic iron oxide. Consequently, the measured diffraction pattern was given by the sum of the background level and the Bragg diffracted intensity of each crystalline phase, weighted according to the phase fractions derived from refined scale parameters. The peak intensity was computed by the crystal structure model (chemical species and atomic positions in the unit cell). The crystallographic data used in the analysis were the following: a unit cell size of 8.268 Å and a $Fd\bar{3}m$ space group for the magnetite; a unit cell size of 8.3457 Å and a $P4_332$ space group for the maghemite; cell parameters $a = b = 3.7852$ Å and $c = 9.5139$ Å and a $I41/am$ space group for the anatase. The domain shape was convoluted with the Bragg reflections to fit the full widths of the peaks. The background was described by a Chebyshev polynomial with refinable coefficients. The accuracy of the weight fraction evaluation was estimated by a goodness of the fit statistical indicator (GoF), which takes the value of 1 for an ideal fit. GoF values of <3−4 were considered satisfactory.[37] The error in the calculated phase fraction value was around ~5%.

Raman Spectroscopy. Raman spectra were recorded by using a Renishaw Invia Raman Microprobe in a backscattering configuration, equipped with a Spectra Physics Ar^+ laser (λ = 514.5 nm), a CCD detector, and a Leica Microscope. A 50× objective was used for the measurements. The samples were prepared by depositing a few drops

(34) Spence, J. *Experimental High-Resolution Electron Microscopy*; Oxford, New York, 1988; p 87.

(35) Carlino, E.; Grillo, V. *Proceedings of the 7th Multinational Congress on Microscopy*; 26−30 June 2005, Portoroz, Slovenia,, 2005; p 6303.

(36) Hÿtch, M. J.; Snoeck, E.; Kilaas, R. *Ultramicroscopy* **1998**, *74*, 131.

(37) (a) Hammersley, A. P.; Svensson, S. O.; Hanfland, M.; Fitch, A. N.; Häusermann, D. *High Pressure Res.* **1996**, *14*, 235. (b) Cervellino, A.; Giannini, C.; Guagliardi, A.; Ladisa, M. *Phys. Rev. B* **2005**, *72*, 35412.

of a concentrated NC solution onto a glass slide and allowing the solvent to evaporate. Acquisition times were typically of the order of 30−60 s.

Mössbauer Spectroscopy. ^{57}Fe Mössbauer transmission spectra were obtained with a conventional spectrometer using a ^{57}Co source of 3.7 GBq mounted on an electromagnetic driving system with a sinusoidal velocity profile. The NC material was mixed with coffee powder and crushed to obtain a sample with homogeneous thickness, which was then sealed in plastic sample holders. For low-temperature measurements either a helium continuous flow or a helium-bath cryostat were used. In both cases, the temperature was controlled at better than ±0.5 K.

Magnetic Susceptibility Measurements. Magnetic characterization was performed with a S600 SQUID magnetometer from Cryogenic Ltd. The NC samples were measured both as diluted $CHCl_3$ solutions and as solid powders obtained by gentle solvent evaporation. Zero-field-cooled (ZFC) and field-cooled (FC) curves were recorded after cooling the sample in the absence or in the presence of a 50 Oe field, respectively. The powder samples were measured in the 2−300 K range, while samples in diluted $CHCl_3$ were measured in the 2−190 K range (i.e., below the fusion temperature of $CHCl_3$, 204 K). Ac susceptibility measurements were performed with a homemade probe inserted in a temperature-variable cryostat from Oxford Co., operating in the 20−25000 Hz range. All data were corrected for the diamagnetic TiO_2 contribution which was independently measured under the same experimental conditions.

3. Results

3.1. Influence of Reaction Conditions. BNCs were synthesized by N_2-protected decomposition of $Fe(CO)_5$ in a OLAC/OLAM/DDIOL mixture in the presence of preformed TiO_2 NRs at $T > 220$ °C. The resulting product was finally exposed to air at 120 °C. The influence of several reaction parameters for the formation of the heterostructures, such as the growth temperature, the absolute reactant concentrations, the TiO_2 to $Fe(CO)_5$ molar ratio, and the TiO_2 seed size, on the growth of the BNCs, was investigated systematically.

Effect of the Reaction Time. The TEM photographs in Figure 1 illustrate the typical temporal evolution of the growth of BNCs synthesized from hydrolytically prepared OLAC-capped TiO_2 NRs.[33a] These TiO_2 seeds (panels a,b**)** possessed an average length of ∼25−30 nm and a diameter of ∼3.5−4 nm. A 10−15% fraction of fork-shaped TiO_2 NRs (i.e., NRs with two arms diverging from a branching point),[38] was also present in the population (see Figure S1 in the Supporting Information for details). At the earliest growth stages (t = 15 min, panels c,d), rodlike NCs were still observable. However, roughly spherical "patches" of ∼3−4 nm that exhibited a slightly different image contrast could be recognized along the NRs. Subsequently (t = 30 min, panels e,f), the samples contained clearly distinguishable binary nanocrystal heterostructures, each comprising a rod section attached to one spherical domain of ∼7−8 nm. At the final stage (t = 60 min, panels g,h), the average size of the spheres had reached ∼12−13 nm, and no further enlargement could be appreciated upon prolonging the heating time. On the basis of such dimensional/topological evolution and on control syntheses in the absence of $Fe(CO)_5$ (see the next paragraphs), it could be preliminarily inferred that the rod-shaped sections in the BNCs were made of TiO_2, whereas the spherical domains were made of iron oxide.

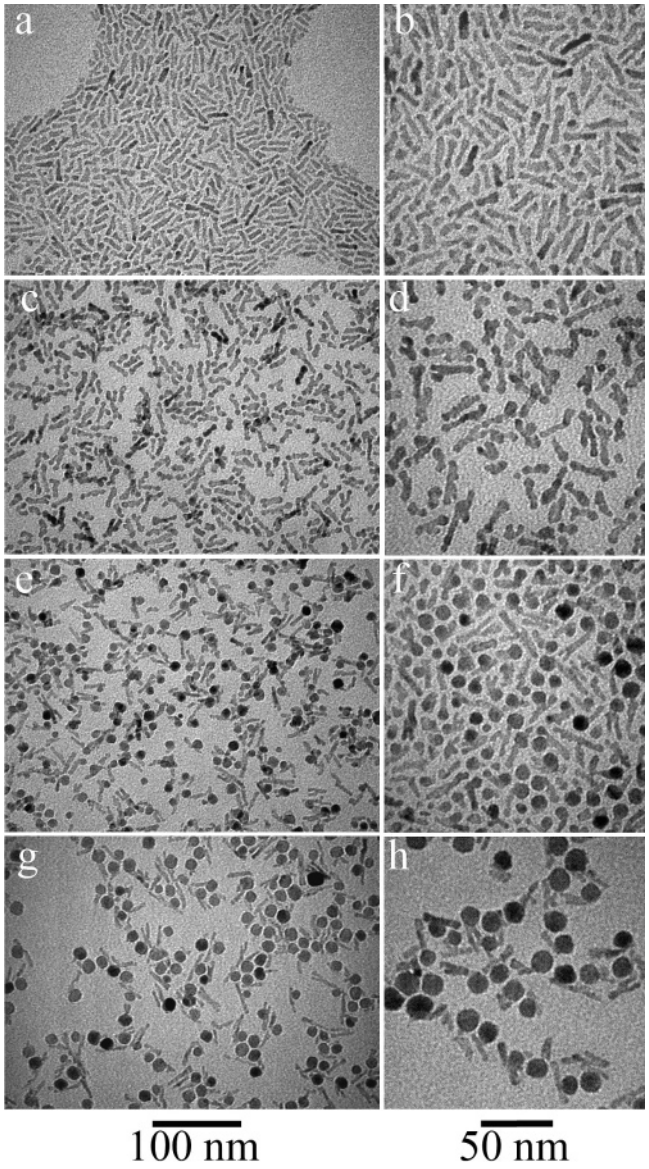

Figure 1. Typical temporal evolution of the heterostructure growth. Low (left panels) and high magnification (right panels) TEM images of hydrolytically prepared TiO_2 seeds before (a,b) and after reaction with $Fe(CO)_5$ at 300 °C: 15 min (c,d); 30 min (e,f); 60 min (g,h). Both the TiO_2 and $Fe(CO)_5$ concentrations were 0.10 M.

Inspection of BNCs under various orientations on the TEM grid revealed that in most cases the iron oxide component could be located at any relative position along the longitudinal sides of the rod sections. Consequently, the projected images of those NRs which carried a sphere attached either to their terminal or to their middle part, exhibited a matchstick- or Ø-shaped profile, respectively, when the plane intersecting both domains was almost parallel to the electron beam. Ternary NCs, i.e., composed of one NR and two spheres, were detected only occasionally.

The following observations suggested the formation of truly TiO_2/iron oxide heterojunctions. First, the BNCs could be selectively destabilized from their nonpolar solution by calibrated addition of a nonsolvent (i.e., a solvent of different polarity, such as an alcohol),[1,2] and therefore they could be effectively separated from both unreacted TiO_2 NRs and iron oxide NCs that had nucleated independently. This result proved

(38) (a) Jun, Y.-w.; Casula, M. F.; Sim, J.-H.; Kim, S. Y.; Cheon, J.; Alivisatos, A. P.; *J. Am. Chem. Soc.* **2003**, *125*, 15981. (b) Chemseddine, A.; Moritz, T. *Eur. J. Inorg. Chem.* **1999**, 235.

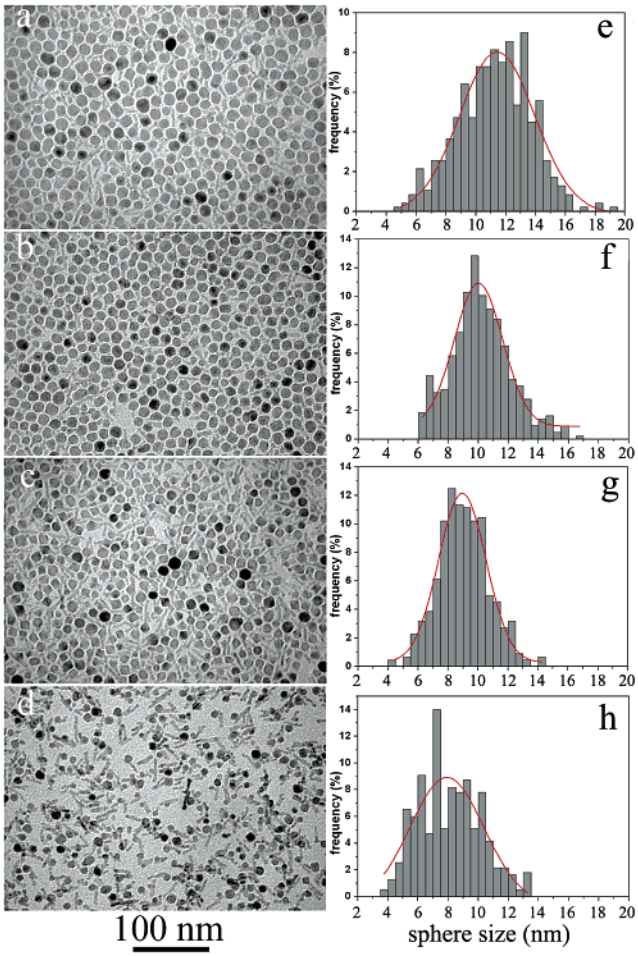

Figure 2. TEM images of size-selected BNCs synthesized at $[TiO_2] = 0.30$ M and $[Fe(CO)_5] = 0.20$ M at different temperatures: (a) 240 °C; (b) 260 °C; (c) 280 °C; (d) 300 °C. From the corresponding statistical analyses in panels e−h, the mean sizes of the iron oxide domains were 11.3 ± 2.4, 10.2 ± 2.0, 9.0 ± 1.7, and 8.1 ± 2.1 nm for a−d, respectively.

that the BNCs were actually the objects with the highest mass in the particle population, as they were composed of permanently linked TiO_2 and iron oxide domains. Second, the statistical analysis over various areas of the TEM grid indicated that the relative ratio between the populations of the two particle types was very close to ∼1. In contrast, when the grid was prepared by depositing mixed solutions of TiO_2 NRs and iron oxide NCs provided by separate syntheses, no attached nanorod/sphere pairs were unambiguously identified. This fact allowed us to rule out that the formation of the BNCs arose from the spontaneous assembly of the particles during evaporation of the solvent from the grid.

Effect of the Temperature. The effect of this parameter on the resulting BNCs is illustrated in Figure 2, which reports the TEM images of size-selected heterostructures grown at various temperatures (in the 240−300 °C range) starting from the same TiO_2 seeds as those shown in Figure 1a,b. In these experiments, a fixed amount of $Fe(CO)_5$ was injected (the final concentration was 0.2 M), while the TiO_2 concentration was set at a relatively high value (≥∼0.30 M) to maximize the probability of heterogeneous nucleation of iron oxide. The BNC yield, i.e., the fraction of NRs that was converted into BNCs in the as-prepared (i.e., not subjected to size-sorting) samples, changed from 35% at 240 °C to 65% at 260 °C, 80% at 280 °C, and 92% at 300 °C. Concomitantly, the relative abundance of isolated iron oxide NCs was seen to increase only slightly, as it remained below ∼20% of the total particle population. Moreover, the mean size of the iron oxide domains in the final BNCs was gradually modulated. For instance, in Figure 2 iron oxide domains of 11.3 ± 2.4, 10.2 ± 2.0, 9.02 ± 1.7, and 8.1 ± 2.1 nm were yielded by syntheses carried out at 240, 260, 280, and 300 °C, respectively, as inferred from the relative statistical data in panels e−h. Almost identical sizes were measured for those iron oxide NCs that had nucleated independently.

Effect of the $Fe(CO)_5$ Concentration. The effect of $Fe(CO)_5$ concentration was examined under the same TiO_2 saturated (≥0.30 M) conditions as those described before. Generally, at a given temperature an increase in the initial $Fe(CO)_5$ amount did not alter the BNC yield to any significant extent; however, it led to comparatively larger iron oxide NCs. At $Fe(CO)_5$ concentrations above ∼0.30 M, the fraction of isolated iron oxide NCs drastically increased over ∼50% of the total particle population.

Effect of the $TiO_2/Fe(CO)_5$ Concentration Ratio. The influence of the NR seed/iron precursor concentration ratio on the features of the resulting heterostructures was clearly disclosed by syntheses in which the TiO_2 loading in the flask was systematically changed (from 0.20 to 0.015 M) at a moderate temperature (270 °C) and low $Fe(CO)_5$ concentration (0.05 M). These conditions guaranteed a nearly constant and elevated BNC yield (higher than 85%) and kept the formation of separate spheres at <10% of the total population. First, it was observed that, at a given temperature and for a fixed amount of $Fe(CO)_5$, the higher the $TiO_2/Fe(CO)_5$ ratio in the flask, the faster the solution darkened, indicating that iron oxide generation was promoted by the TiO_2 seeds. Second, as reported in Figure 3, the progressive reduction in the $TiO_2/Fe(CO)_5$ molar ratio from 4 to 0.3 resulted in the systematic variation of the iron oxide domain size, which could be grown as large as 6.9 ± 1.4 nm (a), 10.1 ± 1.8 nm (b), 13.3 ± 1.9 nm (c), and 17.2 ± 3.0 nm (d), respectively, as deduced from the relative statistical analyses in panels e−h. An analogous trend as a function of the $TiO_2/Fe(CO)_5$ ratio was detected for BNCs provided by syntheses in which increasing amounts of $Fe(CO)_5$ were injected at a fixed TiO_2 content.

Effect of the TiO_2 Nanorod Seed Size. BNCs were successfully synthesized starting from TiO_2 NRs of remarkably larger sizes, that could be prepared as long as ∼50−70 nm and as thick as 5−6 nm by an OLAC/OLAM-assisted nonhydrolytic approach.[33b] An example of heterostructures based on such seeds can be found in Figure S2 of the Supporting Information. Also under these circumstances, a single iron oxide particle domain per nanorod was nucleated on average, and its size could be modulated by adjusting the reaction parameters, according to the criteria illustrated previously.

Control Experiments. For a comparison, several control syntheses were also performed to understand the role of the surfactants and of the seed stability in the heterostructure formation.

Without any organic ligands, the TiO_2 NRs formed large aggregates at high temperature, which ultimately precipitated out of the solution. On one hand, in the presence of OLAC, the TiO_2 NRs remained soluble, but their dimensions were reduced

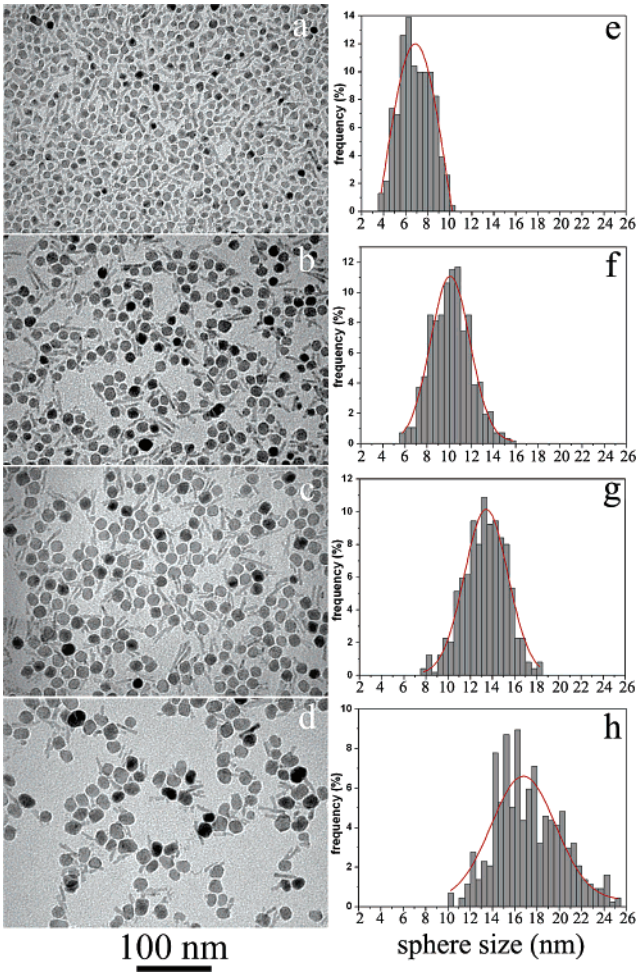

Figure 3. TEM images of as-prepared BNCs synthesized at 270 °C at different TiO_2 seed concentration: 0.20 M (a), 0.10 M (b), 0.05 M (c), 0.015 M (d). The final $Fe(CO)_5$ concentration was 0.05 M. From the corresponding statistical analyses in panels e−h, the mean sizes of the iron oxide domains were 6.9 ± 1.4, 10.1 ± 1.8, 13.3 ± 1.9, and 17.2 ± 3.0 nm for a−d, respectively.

significantly during the heating. On the other hand, the structural/morphological stability of the TiO_2 NRs was preserved when both OLAM and OLAC were present and the growing mixture maintained optical transparency during the syntheses. For any set of conditions, the BNC yield could be increased by 40−50% upon introduction of DDIOL.

Without TiO_2 seeds, decomposition of $Fe(CO)_5$ in the ternary surfactant mixture yielded well-dispersed iron oxide NCs for which size and limited shape control was achieved by adjusting temperature and/or reactant concentration, according to literature criteria.[30,39b] For instance, the slow heating of all reactants to a target temperature led to spherical NCs, whereas the fast injection of $Fe(CO)_5$ into the already hot surfactants yielded faceted objects, exhibiting a diamondlike, hexagonal-, or a triangular-shaped profile, depending on the conditions (Supporting Information, Figure S3).

Finally, any preparation of BNCs by thermal treatment of TiO_2 NRs with preformed iron oxide NCs either with or without added ligands was unsuccessful.

(39) (a) Huber, D. L. *Small* **2005**, *5*, 482. (b) Casula, M. F.; Jun, Y.-w.; Zaziski, D. J.; Chan, E. M.; Corrias, A.; Alivisatos, A. P. *J. Am. Chem. Soc.* **2006**, *128*, 1675.

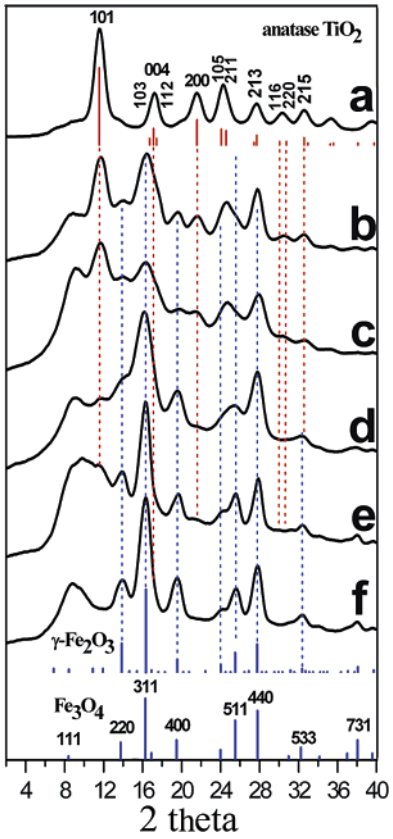

Figure 4. Powder X-ray diffraction patterns of: (a) 3.5 nm × 30 nm TiO_2 NRs (corresponding to Figure 1a,b); (b−e) TiO_2/iron oxide BNCs grown from these seeds (corresponding to Figure 3a−d, respectively); (f) ∼8 nm iron oxide NCs. The percentage phase compositions of samples b−e, estimated by fitting the patterns with a WPPT approach, were better described as γ-Fe_2O_3:TiO_2 mixtures: (b) 33:67; (c) 51:49; (d) 66:34; (e) 90:10, respectively.

3.2. Characterization of Nanocrystal Ensembles. X-ray Diffraction Analysis. In Figure 4, the measured powder XRD patterns of the initial TiO_2 NRs (corresponding to Figure 1a,b), of BNCs with different mean iron oxide size grown from these NRs (corresponding to Figure 3a,d, respectively), and of ∼8 nm iron oxide NCs are reported. The profile of the TiO_2 NRs (trace a) was unambiguously indexed to the anatase polymorph, although crystal shape anisotropy could not be estimated from inhomogeneous peak width[33] due to intrinsic limits of the instrumental resolution function. The pattern of pure iron oxide NCs (trace f) was attributable to the cubic spinel structure of both γ-Fe_2O_3 (maghemite) and Fe_3O_4 (magnetite), or to a mixture of both phases, which could not be discriminated owing to the significant line broadening. The XRD patterns of the BNCs (traces b−e**)** were consistent with the presence of both the anatase and the cubic spinel structures. The complex modification in the relative intensities and widths of the respective reflections suggested that the samples contained the two phases in different relative proportions. This fact was clearly disclosed by the analysis of those peaks of the respective phases which merged only little with each other. For instance, from b to e, a gradual intensity decrease for the {101}, {004}, and {200} reflections of anatase was accompanied by the progressive growth of the {220}, {311}, and {400} reflections of the cubic spinel structure. Similar behavior was recorded for samples that were not subjected to the air-oxidation step.

The quantification of the sample composition was performed by fitting the data with WPPF software, assuming either a TiO_2/γ-Fe_2O_3, a TiO_2/Fe_3O_4, or a $TiO_2/Fe_3O_4/\gamma$-Fe_2O_3 mixture. Within the approximation of our calculation model, the BNC samples were better described by a TiO_2/γ-Fe_2O_3 combination. For instance, the maghemite/anatase percentages deduced from the XRD data in Figure 4 were found to be: 33:67, 51:49, 66:34, 90:10, respectively. As expected, the fraction of the spinel structure scaled up with the proportional increase in both the mean size and the relative population of the iron oxide domains (including the separated spheres) over that of the TiO_2 NRs. We compared these fitting results with an indirect estimation of phase abundance done on the basis of the statistical TEM analysis of the samples. From the average particle diameter, and from the density of bulk anatase TiO_2 (which is 4.23 g/cm^3) and of bulk γ-Fe_2O_3 (4.88 g/cm^3), the average mass of a single NC was calculated. For example, a mass of 4.41×10^{-18} g and of 2.03×10^{-18} g, was calculated for a γ-Fe_2O_3 sphere of 12 nm and for a TiO_2 NR of 4 nm $\times$ 4 nm $\times$ 30 nm, respectively. The TEM-derived particle type composition was then translated into a crystalline phase composition. The agreement with the XRD-calculated composition was within 5−10%, hence, of the same order of the standard deviation error of the WPPF fitting procedure.

Raman Spectroscopy. The composition of the BNCs was further assessed by Raman spectroscopy. The Raman scattering efficiency as well as the relative band intensities is characteristic of each material, but depends sensitively also on the sample characteristics (e.g., local lattice imperfections, surface status), and the excitation wavelength.[40−42] As compared to the corresponding bulk counterparts, NCs exhibit blue-shifted Raman bands and larger linewidths as a consequence of phonon confinement.[40−42] Therefore, the Raman spectra of bare TiO_2 NRs and of pure iron oxide NCs were first measured independently at various laser powers, and used as references to interpret the data relative to the BNCs (see Supporting Information, Figures S4, S5). The excitation of the TiO_2 phonon modes required a comparatively higher laser intensity than that necessary to detect signals of iron oxide, at which a transformation of the spinel cubic phase of γ-Fe_2O_3/Fe_3O_4 into the hexagonal α-Fe_2O_3 (hematite) occurred. As an example, Figure 5 reports the Raman spectra of a heterostructure sample (corresponding to Figure 3c) recorded under different excitation conditions. At low laser power (1.25 mW, top panel), only three rather broad and weak bands, centered at ~320, ~540, and ~675 cm^{-1}, respectively, were detected and ascribed to γ-Fe_2O_3 and/or Fe_3O_4.[40,41] At higher laser power, (12.5 mW, bottom panel), anatase TiO_2 was identified by the narrow signals[42] at ~200, ~410, and the shoulder at ~640 cm^{-1}. The narrow peaks at ~220, ~293, and ~600 cm^{-1} were ascribed to α-Fe_2O_3 resulting from the laser-induced transformation of γ-Fe_2O_3/Fe_3O_4. The peaks at ~350 and ~665 cm^{-1} could be due to residual spinel cubic phase. As the light-driven γ-Fe_2O_3/Fe_3O_4 to α-Fe_2O_3 conversion is quite distinctive,[40,41] it can serve as a valuable diagnostic tool, which can indirectly confirm the presence of spinel cubic iron oxide phase in the as-prepared BNCs, in agreement with the XRD data. Similar results were obtained for BNCs that were not subjected to the air-exposure step and/or that carried iron oxide domains of different sizes.

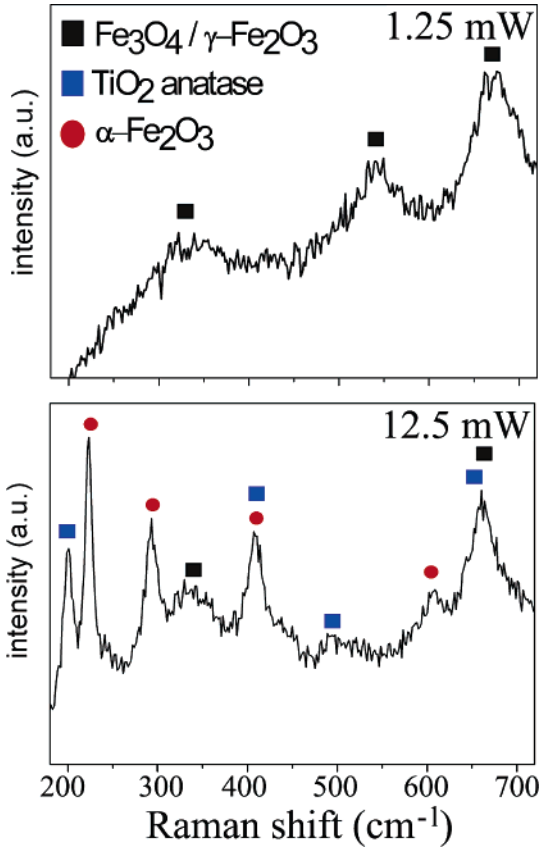

Figure 5. Raman spectra (λ_{ex} = 514.5 nm) of TiO_2/iron oxide binary nanocrystals (corresponding to Figure 3c) recorded at different laser powers: (top) 1.25 mW; (bottom) 12.5 mW.

Magnetic Characterization. In panel a of Figure 6, the temperature dependence of the magnetic susceptibility χ recorded under zero-field/field cooling conditions is reported for two representative BNC powders, synthesized according to the same protocol as that used for samples in Figure 3. The investigated BNCs, that herein are referred to as S1 and S2 for sake of clarity, carried iron oxide domains of 4.1 ± 0.6 nm and 10.7 ± 2.1 nm, respectively, as measured by TEM. The average blocking temperature, T_B, above which the system behaves as superparamagnet, can be identified with the temperature at which the total ZFC magnetization reaches its maximum. Owing to the presence of size distribution for the magnetic iron oxide domains, T_B lies between T_{sat} (saturation temperature in the FC curve) and T_{irr} (irreversible temperature, at which the ZFC and FC curves coincide). In panel a, the susceptibility behaviors of the samples appear similar, and the measured values of T_B are 36 and 87 K for S1 and S2, respectively. Overall, these results

(40) (a) Lottici, P.; Baratto, C.; Bersani, D.; Antonioli, G.; Montenero, A.; Guarneri, M. *Opt. Mater.* **1998**, *9*, 368. (b) Sousa, M. H.; Tourinho, F. A.; Rubim, J. C. *J. Raman Spectrosc.* **2000**, *31*, 185.
(41) (a) de Faria, D. L. A.; Venancio Silva, S.; de Oliveira, M. T. *J. Raman Spectrosc.* **1997**, *28*, 873. (b) Chourpa, I.; Douziech-Eyrolles, L.; Ngaboni-Okassa, L.; Fouquenet, J.-F. ; Cohen-Jonathan, S. ; Soucé, M. ; Marchais, H. ; Dubois, P. *Analyst* **2005**, *10*, 1395. (c) Pinna, N.; Grancharov, S.; Beato, P.; Bonville, P.; Antonietti, M.; Niederberger, M. *Chem. Mater.* **2005**, *17*, 3044.
(42) (a) Zhang, W. F.; He, Y. L.; Zhang, M. S.; Yin, Z.; Chen, Q. *J. Phys. D: Appl. Phys.* **2000**, *33*, 912. (b) Zhang, J.; Li, M.; Feng, Z. ; Chen, J.; Li, C. *J. Phys. Chem. B* **2006**, *110*, 927.
(43) (a) Fiorani, D., Ed. *Surface Effects in Magnetic Nanoparticles*; Springer: New York, 2005. (b) Batlle, X.; Labarta, A. *J. Phys. D: Appl. Phys.* **2002**, *35*, R15.
(44) (a) Dormann, J. L.; Bessais, L.; Fiorani, D. *J. Phys. C: Solid State Phys.* **1988**, *21*, 2015. (b) Dormann, J. L.; Fiorani, D.; Tronc, E. In *Magnetic Relaxation in Fine-Particle Systems*; Prigogine, I., Rice, A., Eds.; Advances in Chemical Physics, Vol. 98; John Wiley & Sons: New York, 1997. (c) Kodama, R. H. *J. Magn. Magn. Mater.* **1999**, *200*, 359.

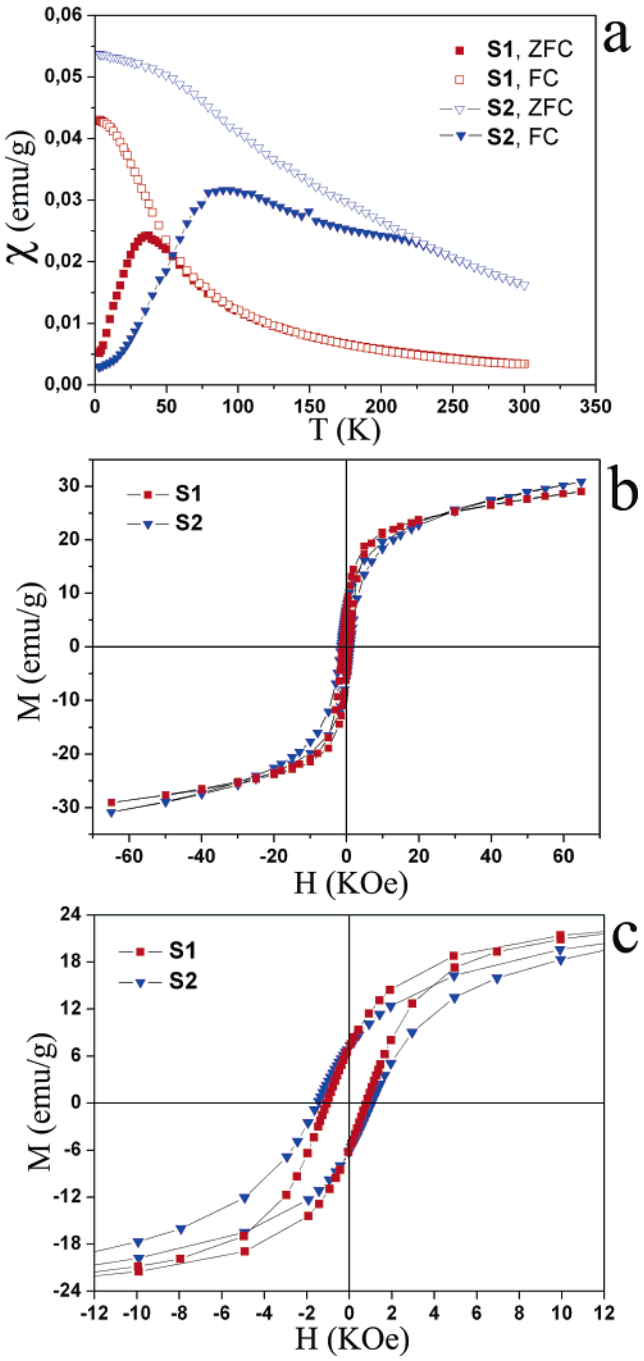

Figure 6. (a) ZFC/FC curves and (b,c) hysteresis loops at 2.5 K of two BNC powder samples (the mean iron oxide domain size is 4.1 ± 0.6 nm for S1 and 10.7 ± 2.1 nm for S2. The magnetization M and magnetic susceptibility χ are per gram of iron oxide. The residual magnetization and the coercive field in panel (b) are evidenced in the expanded view in (c).

are consistent with the Néel model, which predicts that T_B will scale up with the NC magnetic volume, V_{NC}:[43,44]

$$T_B = \frac{K_A V_{NC}}{k_B \ln(\tau_m/\tau_0)} \qquad (3)$$

where K_A is the anisotropy constant, k_B is the Boltzmann constant, V_{NC} is the NC magnetic volume, and τ_m and τ_0 are the measuring time and attempt time, respectively.

The hysteresis loops recorded between −65 kOe and +65 kOe at 2.5 K are shown in panels b,c. It should be noted that in both cases the loop was recorded after field cooling the samples through the blocking temperature with a +50 Oe field. As a general feature, the curves do not reach saturation, and the saturation magnetization (M_S) values fall below that of bulk cubic spinel iron oxide (around 80−85 emu/g).[30,43,44] The M_S values, estimated by fitting the high field data using the empirical formula: $M = M_S + a/H + b/H^2$, were 36 emu/g and 41 emu/g for S1 and S2, respectively. It is known that iron oxide NCs are often characterized by a spin-disordered surface layer. The reduced coordination number of surface atoms can favor spin configurations different from the fully aligned one, introducing disorder and frustration which may give rise to spin-glasslike behavior.[43] This explains why the BNCs with smaller iron oxide domains (and hence with greater surface/volume ratios) exhibited lower M_S values. The fact that the curves do not become flat at saturation manifests the progressive alignment of such spin-disordered phases with the external field.

The residual magnetization, M_R, is about 7.2 emu/g in both samples, while the coercive field, H_C, is as high as 910 and 1270 Oe for S1 and S2, respectively. The whole loops are not symmetric but are shifted toward negative field values by about ∼160−200 Oe. Such displacements can be accounted for by again invoking the different magnetic behavior of surface and core atoms in NCs. The iron oxide domains in the BNCs can be described as being made of an ordered core surrounded by a disordered, spin-glasslike shell. The field cooling procedure selects and "freezes" a metastable surface spin configuration, resulting in a net magnetic moment along the field direction. Therefore, the coupling of this frozen glasslike surface spin layer with the core would produce an additional anisotropy term which makes alignment of the core magnetic moment along the field-cooled direction more favorable. In order to verify this hypothesis, the hysteresis loops measurements were repeated after cooling the samples under a larger magnetic field (65 kOe). As expected, the hysteresis negative shift increased up to 450−490 Oe.

Except for a scale factor due to the undefined particle concentration, no significant alterations in the shape of the ZFC/FC curves nor in the hysteresis loops were observed when the BNCs were measured as diluted $CHCl_3$ solutions (see Figure S6 in the Supporting Information). This fact indicated that interparticle interactions were not relevant in determining the magnetic properties of the BNCs.[43,44]

The dynamics of the magnetization reversal was investigated by measuring the temperature dependence of the ac susceptibility at different frequencies of the driving alternate magnetic field.[45] According to the Néel model, the T_B value measured at a given working frequency υ, $T_B(\upsilon)$, is related to υ by the following expression:

$$\ln \tau_m = \ln 1/2\pi\upsilon = \ln \tau_0 + K_A V_{NC}/k_B T_B(\upsilon) \qquad (4)$$

$T_B(\upsilon)$ can be obtained by assuming that at the maximum of the out-of-phase component of the susceptibility, χ'', the relaxation time of the magnetic moments matches with the measuring time τ_m. Therefore, the attempt time τ_0 and the anisotropy constant K_A were determined by a fitting procedure after recording both

(45) (a) Buscher, K.; Helm, C. A.; Gross, C.; Glockl, G.; Romanus, E.; Weitschies, W. *Langmuir* **2004**, *20*, 2435. (b) Rondinone, A. J.; Liu, C.; Zhang, Z. J. *J. Phys. Chem. B* **2001**, *105*, 7967. (c) Zhang, J.; Boyd, C.; Luo, W. *Phys. Rev. Lett.* **1996**, *77*, 390.

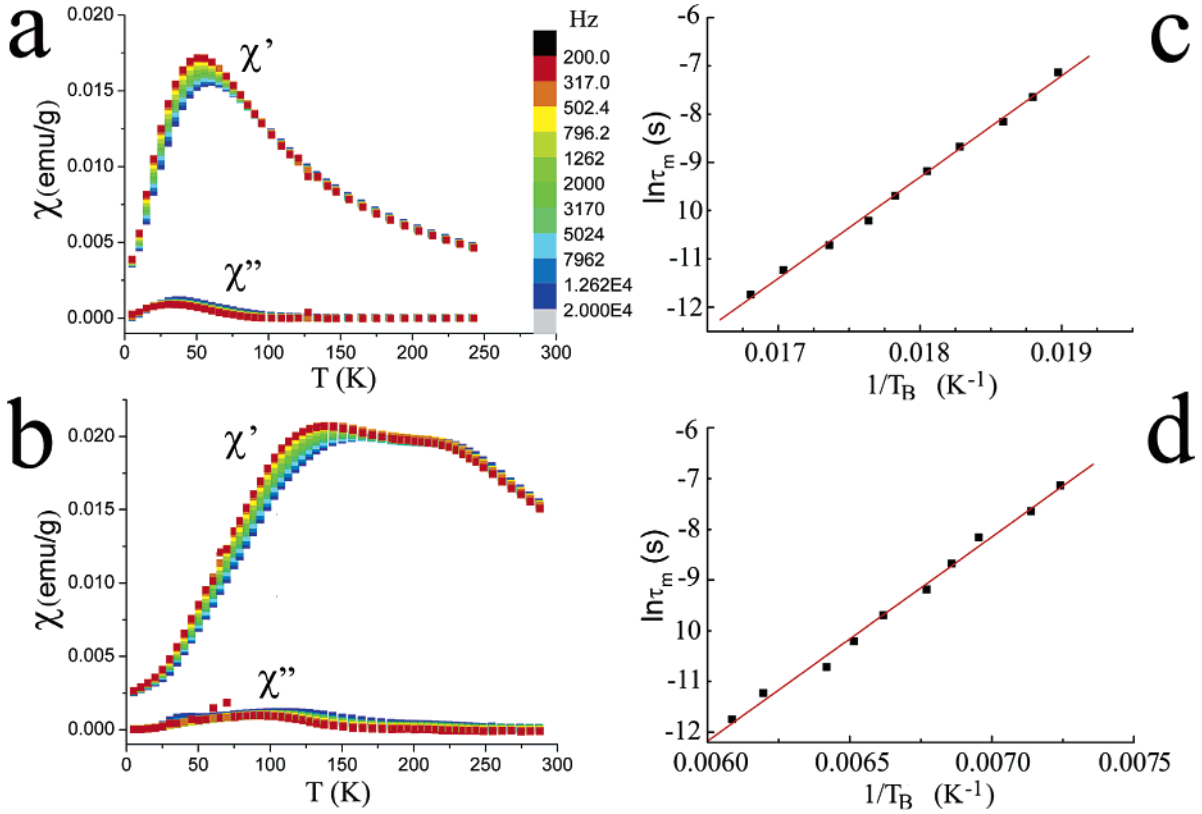

Figure 7. (a,b) Temperature-dependent ac magnetization susceptibility measured at various frequencies for the heterostructure samples S1 and S2, respectively. (c,d) Variation of the measuring time τ_m as a function of the blocking temperature $T_B(\upsilon)$ for S1 and S2, respectively.

χ'' and the in-phase component of the susceptibility, χ', as a function of temperature at 10 logarithmic-spaced frequencies in the 200−20000 Hz range. The respective χ' and χ'' curves recorded for S1 and S2 are presented in Figure 7, together with the respective ln τ_m vs $1/T_B(\upsilon)$ plots. The fits exhibited the expected linear behavior. The best fit parameters obtained were: $\tau_0 = 10^{-20.4}$ s and $K_A V_{NC}/k_B = 2097$ K for S1, and $\tau_0 = 10^{-15.8}$ s and $K_A V_{NC}/k_B = 4022$ K for S2. By using the mean NC size value obtained by TEM, K_A was estimated to be 0.8 and 0.1 MJ m^{-3}, for Sl and S2, respectively, therefore higher than the bulk value (about 0.01−0.1 MJ m^{-3} for magnetite and 0.1 MJ m^{-3} for maghemite). Moreover, the T_B(S1)/T_B(S2) ratio deduced from ac data agrees well with that measured by the ZFC/FC techniques. This finding confirms that the magnetic anisotropy is size-dependent. In particular, the larger value measured for the BNCs with smaller iron oxide domains reveals the fundamental role played by the surface in determining the total magnetic anisotropy of the material. The measured T_B and K_A values are similar to those previously detected for other weakly interacting iron oxide NCs.[30] The diamagnetic contribution of the TiO_2 NRs was measured separately and found negligible with respect to the magnetization values of sample S1 and S2 under all the experimental conditions applied. Unfortunately, however, any detailed comparison with iron oxide NCs synthesized without TiO_2 was inadequate, as these NCs exhibited different mean size and/or size distributions, shape, and phase compositions (a magnetite fraction was present), as supplemented elsewhere (Supporting Information, Figures S3 and S8 and Table S1).

Mössbauer Spectroscopy. To discriminate between the maghemite and magnetite phase in the BNCs, ^{57}Fe Mössbauer spectroscopy measurements were performed. Figure 8 reports the temperature-dependent Mössbauer spectra along with the respective fits for two representative BNCs, synthesized under the same general conditions as those employed for samples in Figure 3. The investigated BNCs, that herein are referred to as M1 and M2 for sake of clarity, carried average iron oxide domains of 7.6 ± 2.1 nm and 10.9 ± 3.6 nm, respectively, as determined by TEM. For these samples, the Mössbauer absorption lines exhibit broad widths, and their shapes significantly deviate from the Lorentzian type. The asymmetrical line broadening, already evident in the spectra at $T = 6$ K, points to an asymmetric distribution of magnetic hyperfine fields, arising from the different configurations of Fe in the core and on the surface of the iron oxide domains.[46a,b] At elevated temperatures, a component exhibiting superparamagnetic relaxation is observable, as the magnetic moments can flip between the two easy magnetization directions at 0° and at 180°. Under these circumstances, the magnetic field collapses for a fraction of Fe nuclei, and a doublet appears, which is due to the electric field gradient at the Fe sites. The other Fe nuclei experience the magnetic field and are responsible for the distributed sextet. Therefore, the distinct doublet detected at higher temperatures was considered as an additional superparamagnetic doublet.

The spectra were fitted by using the parameters obtained for reference materials (namely bulk magnetite, maghemite, and hematite) and scaling the hyperfine field, B, by a factor $x = B_{sample}/B_{bulk}$, to take into account the fact that B has a reduced value than that in the bulk (Supporting Information, Figures S7 and S8 and Table S1). Due to the line broadness and asymmetry, a single scale factor approach was inadequate to interpret the spectra. In the lack of a reliable theoretical model,

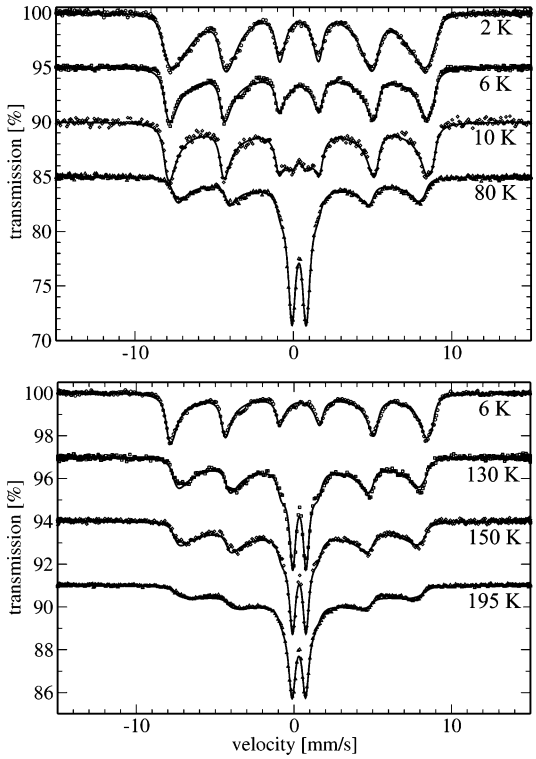

Figure 8. Temperature-dependent Mössbauer transmission spectra (open symbols) and the corresponding fits (solid lines) for two representative BNC samples with iron oxide domains of 7.6 ± 2.1 nm (sample M1, top panel) and 10.9 ± 3.6 nm (sample M2, bottom panel), respectively. The fits were obtained by a phenomenological approach, scaling the hyperfine magnetic field B_{bulk} by a log-normal distribution of scaling factors, as described in the Supporting Information. An additional quadrupole splitting was introduced for the M1 spectra at 6, 10, and 80 K, and for the M2 spectra at 130, 150, and 195 K.

a phenomenological fit of the data was obtained by scaling B_{bulk} by a log-normal distribution of scaling factors x, while still using the other parameters of the bulk materials.[46−48] The resulting values of isomer shift and quadrupole splitting of the superparamagnetic states (Figures S9 and S10 and Table S2 in the Supporting Information) matched well with those reported in the literature for γ-Fe_2O_3.[46b,c,47] Due to the smearing effect of the B distribution, any eventual minor content of magnetite in the samples could not be completely ruled out. From the Mössbauer analysis of Figure 8, it can be therefore concluded

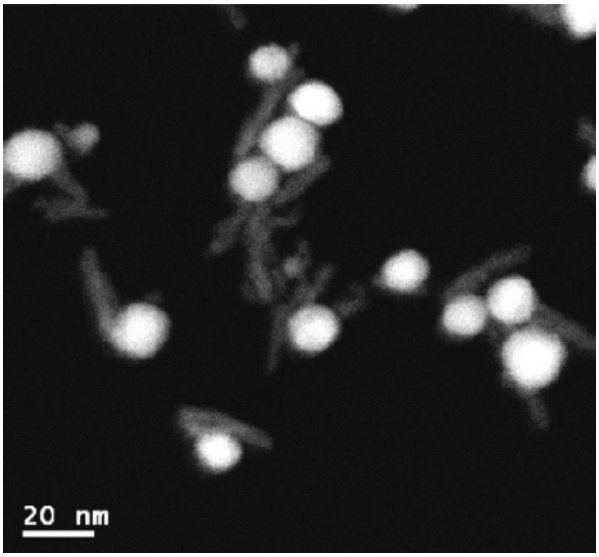

Figure 9. Low-magnification HAADF image of a group of BNCs, including some isolated NCs.

that the iron oxide domains in the BNCs were composed mainly of maghemite, irrespective of their mean size. Finally, although the employed fitting was phenomenological, it provided useful information about the temperature dependence of the paramagnetic and superparamagnetic fractions, from which T_B could be estimated, in good agreement with the ac susceptibility data (Supporting Information, Figures S11 and S12).

3.3. Structural Characterization of Single Nanocrystals. To elucidate the compositional nature and the crystalline structure of individual BNCs, and to gain insight into the heteroepitaxial growth mechanism, detailed TEM−STEM analyses were carried out.

STEM−High-Angle Annular Dark-Field (HAADF) Imaging. Figure 9 is a representative HAADF image of a group of BNCs, showing rod-shaped and spherical objects. The intensity of the HAADF image is strongly related to the mean atomic number of the specimen and to its thickness.[49] Hence, the two particle families in the image are clearly different in composition: the brighter spherical domains are made of iron oxide, whereas the darker NRs are made of TiO_2. Notably, whereas isolated NRs were mainly straight, most of the rodlike sections in the BNCs appeared slightly bent or bowed toward the sphere domain, approximately adapting to its curvature.

Phase Contrast, High-Resolution TEM (HRTEM). HRTEM investigations gave a more detailed picture of the structure

(46) (a) An, S. Y.; Shim, I.-B.; Kim, C. S. *J. Appl. Phys*. **2005**, *97*, 10Q909. (b) Bødker, F.; Mørup, S. *Europhys. Lett.* **2000**, *52*, 217. (c) Bødker, F.; Kochet, C. B.; Hansen, M. F.; Lefmann, K.; Mørup, S. *Phys. Rev. B* **2000**, *61*, 6826. (d) Panda, R. N.; Gajbhiye, N. S.; Balaji, G. *J. Alloys Compd.* **2001**, *326*, 50. (e) Hartridge, A.; Bhattacharya, A. K.; Sengupta, M.; Majumdar, C. K.; Das, D.; Chintalapudi, S. N. *J. Magn. Magn. Mater*. **1997**, *176*, L89. (f) Tronc, E.; Ezzir, A.; Cherkaoui, R.; Chanéac, C.; Noguès, M.; Kachkachi, H.; Fiorani, D.; Testa, A. M.; Grenèche, J. M.; Jolivet, J. P. *J. Magn. Magn. Mater*. **2000**, *221*, 63. (g) Mørup, S.; Tronc, E. *Phys. Rev. Lett.* **1994**, *72*, 3278.

(47) (a) Predoi, D.; Kuncser, V.; Tronc, E.; Nogues, M.; Russo, U.; Principi, G.; Filoti, G. *J. Phys. Condens. Matter* **2003**, *15*, 1797. (b) Tueros, M. J.; Baum, L. A.; Borzi, R. A.; Stewart, S. J.; Mercader, R. C.; Marchetti, S. G.; Bengoa, J. F.; Mogni, L. V. *Hyperfine Interact.* **2003**, *148−149*, 103. (c) Dormann, J. L.; D'Orazio, F.; Lucari, F.; Tronc, E.; Prenè, P.; Jolivet, J. P.; Fiorani, D.; Cherkaoui, R.; Nourgès, M. *Phys. Rev. B* **1996**, *53*, 14291.

(48) (a) Tronc, E. ; Prenè, P. ; Jolivet, J. P.; D'Orazio, F. ; Lucari, F. ; Fiorani, D. ; Godinho, M.; Cherkaoui, R. ; Nougues, M. ; Dormann, J. L. *Hyperfine Interact.* **1995**, *95*, 129. (b) Mørup, S.; Dumesic, J. A.; Topsøe, H. In *Applications of Mössbauer Spectroscopy*; Cohen, R. L., Ed.; Academic Press: New York, 1980; Vol. II, pp 1−53. (c) Kilcoyne, S. H.; Cywinski, R. *J. Magn. Magn. Mater*. **1995**, *140*−144., 1466. (d) Mørup, S.; Bødker, F.; Hendriksen, P. V.; Linderoth, S. *Phys. Rev. B* **1995**, *52*, 287. (e) Cannas, C.; Concas, G.; Gatteschi, D.; Falqui, A.; Musinu, A.; Piccaluga, G.; Sangregorio, C.; Pano, G. *Phys. Chem. Chem. Phys.* **2001**, *3*, 832.

(49) (a) Pennycook, S. J.; Jesson, D. E. *Ultramicroscopy* **1991**, *37*, 14. (b) Nellist, D.; Pennycook, S. J. *Ultramicroscopy* **1999**, *78*, 111.

(50) (a) To the extent of HRTEM analysis, the orthorhombic Fe_3O_4 and the spinel cubic Fe_3O_4 (magnetite) are practically indistinguishable. However, it is known that cubic Fe_3O_4 transforms into the orthorhombic Fe_3O_4 only at a characteristic temperature (see refs 50b−f) of around 125 K (referred to as the Verwey transition). Therefore, the presence of the orthorhombic phase can be ruled out. (b) Redl, F.; Black, C.; Papaefthymiou, G. C.; Sandstrom, R.; Yin, M.; Zeng, H.; Murray, C.; O'Brien, S. *J. Am. Chem. Soc.* **2004**, *126*, 14583. (c) Markovich, G.; Fried, T.; Poddar, P.; Sharoni, A.; Millo, O. *Mater. Res. Soc. Symp. Proc.* **2003**, *746*, Q4.1. (d) Poddar, P.; Fried, T.; Markovich, G. *Phys. Rev. B* **2002**, *65*, 172405. (e) Millot, G.; Keller, N.; Perriat, P. *Phys. Rev. B* **2001**, *64*, 12402. (f) Walz, F. *J. Phys.: Condens. Matter* **2002**, *14*, R285. (g) Note that the γ-Fe_2O_3 basic structure, which is very close to that of cubic spinel structure, should be rigorously considered tetragonal as $a = b = 8.3396$ Å and $c = 8.3221$ Å (see ref 50h). Hereafter, for sake of simplicity, we will use the cubic notation for both magnetite and maghemite, taking into account that the transformation from the tetragonal to the cubic notation requires a 45° rotation of the reference axes. (h) Shmakov, A. N.; Kryukova, G. N.; Tsybulya, S. V.; Chuvilin, A. L.; Solovyeva, L. P. *J. Appl. Crystallogr*. **1995**, *28*, 141.

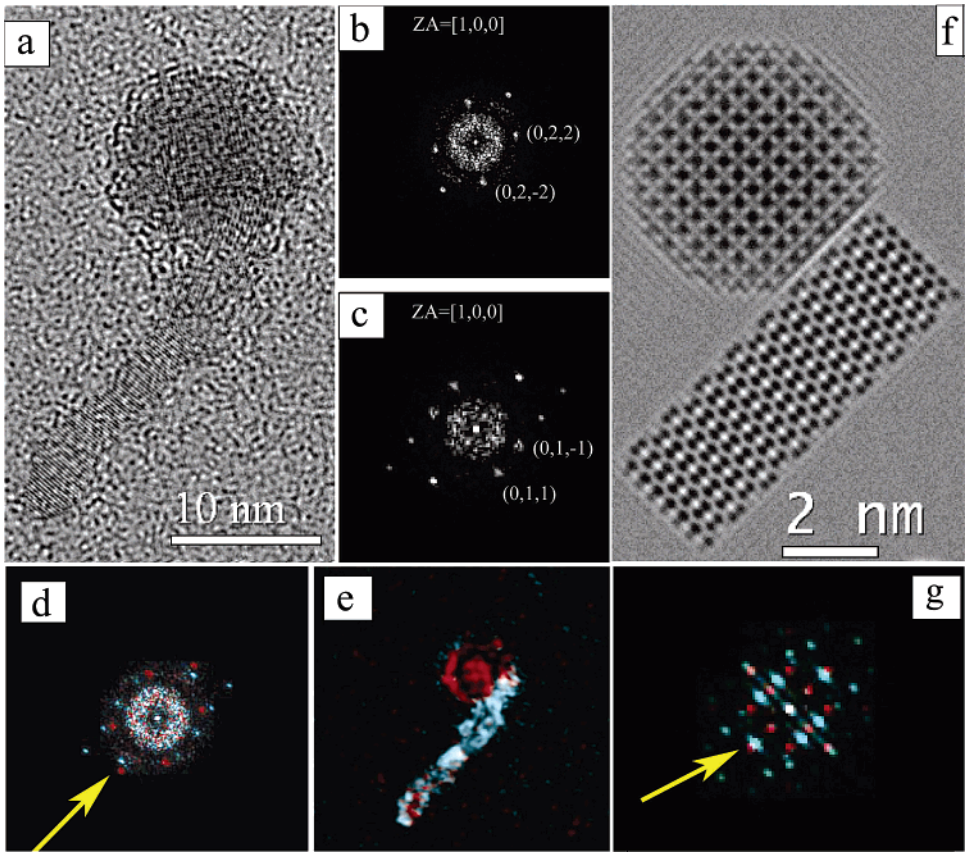

Figure 10. (a) HRTEM image of a single TiO_2/iron oxide BNC. (b,c) Diffractograms obtained from the spherical and the rodlike domain in (a), respectively. (d) Merging of the two diffractograms in (b) and (c), each traced by a different color; the couple of fringes that should be corresponding for a perfect epitaxy are evidenced by an arrow. (e) False color map obtained by periodicity analysis of the image in panel (a): the red color is related to the amplitude of the {022} fringes of maghemite, while the blue color refers to the {011} fringes of anatase. (f) HRTEM simulation for a simplified interface model: the two domains are roughly positioned as in (a). (g) Relevant joint diffractograms relative to (f). In particular, the couple of fringes that should be corresponding for a perfect epitaxy are evidenced by an arrow.

of the BNCs. Unfortunately, in most cases the random orientations of the iron oxide clusters did not allow us to distinguish between cubic spinel magnetite and maghemite phases.[50] Figure 10 shows a typical HRTEM image of a single BNC (panel a) along with the diffractograms for the spherical domain and the rodlike section (panels b,c, respectively). The FFT analyses reveal that the spherical head of the heterostructure is indeed made of either maghemite or magnetite in its ⟨100⟩ zone axis, while the NR is made of *c*-axis elongated anatase TiO_2 in its ⟨100⟩ zone axis (see also Figure S1 in the Supporting Information). The two diffractograms have been merged in panel d to study the relationships between the two lattices. The joint diffractogram shows that the two domains do not have a simple epitaxial connection. A careful inspection of panel a in Figure 10 indicates that the interface between the two particles is close to the {040} plane of maghemite and to the {040} plane of anatase. However, the respective lattice spacings in the relevant orthogonal directions, namely the {004} in maghemite and the {004} in anatase, are not co-incident as should occur in a simple planar epitaxial relationship. A less restrictive relation of epitaxy can be defined, which would simply require the continuity of atomic planes at the interface. For the latter condition to be fulfilled, the *K* vectors of the periodicities of the two crystals should have a common projection on the interface. However, neither is realized with an interface of the same type as that reported in Figure 10. This finding is common to most of the analyzed heterostructures: the interface is often on a low-index crystallographic plane, but a straightforward epitaxial relationship is missing. Despite this, no amorphous layer can be recognized at the junction between the two materials within the limits of the HRTEM observation.

It is worth noting that in the BNC the relative intensities of the lattice fringes change along the rod section, indicating that the latter is slightly distorted in proximity of the iron oxide sphere. Such lattice deformation has never been observed in isolated NRs. These facts strongly support the existence of a genuine inorganic junction between the two materials. To elucidate the bonding relationship, a map of the spatial distribution of the two phases was obtained by analyzing the local amplitude of the respective periodicities (see Experimental Section for details). Panel e in Figure 10 is the color elaboration of the image in panel a. The blue color marks the regions where the {011} fringes of anatase are visible, while the red color refers to the regions where the {022} fringes of maghemite are observable. The spurious red spots on the rod are due to the {011} fringes of anatase which are indeed close to the {022} fringes of maghemite (the cross contribution can be reduced but not completely excluded). While confirming a lattice distortion in the NR section, this phase map additionally suggests that the interface between the two domains is not flat but follows the curvature of the spherical head.

A simplified model of the interface is shown in the HRTEM simulation in panel f along with the relevant diffractograms in panel g. The two Fourier peaks, corresponding to the {040}

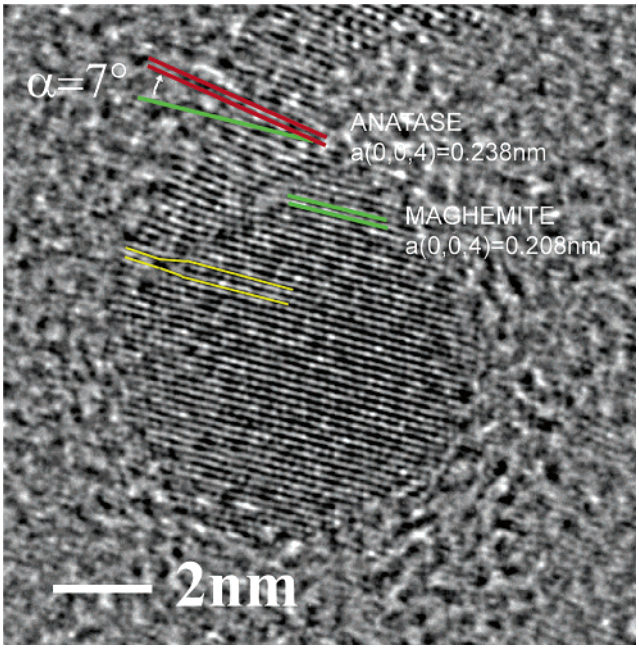

Figure 11. HRTEM image of the junction between an anatase nanorod in the ⟨100⟩ zone axis, and a maghemite sphere in the ⟨130⟩ zone axis. The {004} fringes of anatase are tilted by about 7° to match with the {004} planes of the iron oxide particle. In addition, a dislocation is marked in yellow on the right side of the interface

planes for the respective structures, are highlighted by an arrow in panel g and correspond to the same features as those highlighted in the joint diffactogram in panel d. For a perfect epitaxy to occur, these peaks should be co-incident or should at least have the same projection on the interface. From the simulation it emerges that the two domains cannot be coherently joined together, unless the respective lattices are distorted. Other interface planes, close to the {040} planes, can be considered for the simulation, but in no case can a straightforward epitaxial relationship be found. These results are therefore fully consistent with the previous analysis of the experimental image. Actually, the presence of a crystal deformation at the junction region explains why in most of the cases the identification of which lattice planes are involved in the interface formation is practically impossible to achieve.

Further confirmation for the interface structure can be drawn from the analysis of the BNC in Figure 11. In the observed projection, it can be measured that the {004} anatase fringes approaching the heterostructure interface are tilted by about 7° before matching with the relevant {004} fringes of iron oxide. Furthermore, the presence of a dislocation can be observed at the edges of the spherical domain.

Additional interesting features were detected in heterostructures of the type shown in Figure 12. In panel a, a NR with a branching point can be observed with two separated arms attached to a sphere. The two arms, however, exhibit different inclinations, since the visible fringes are different. In particular, the {011} fringes appear in the upper branch and the {01−1} fringes in the lower one. In both cases, the interfaces are parallel to the anatase {011} planes. This fact has been better evidenced by the false color periodicity analysis reported in panel b. The image shows that the two arms (in red and blue) are touching the sphere (green) on different regions. This evidence can be considered an indication that also in this case the junction

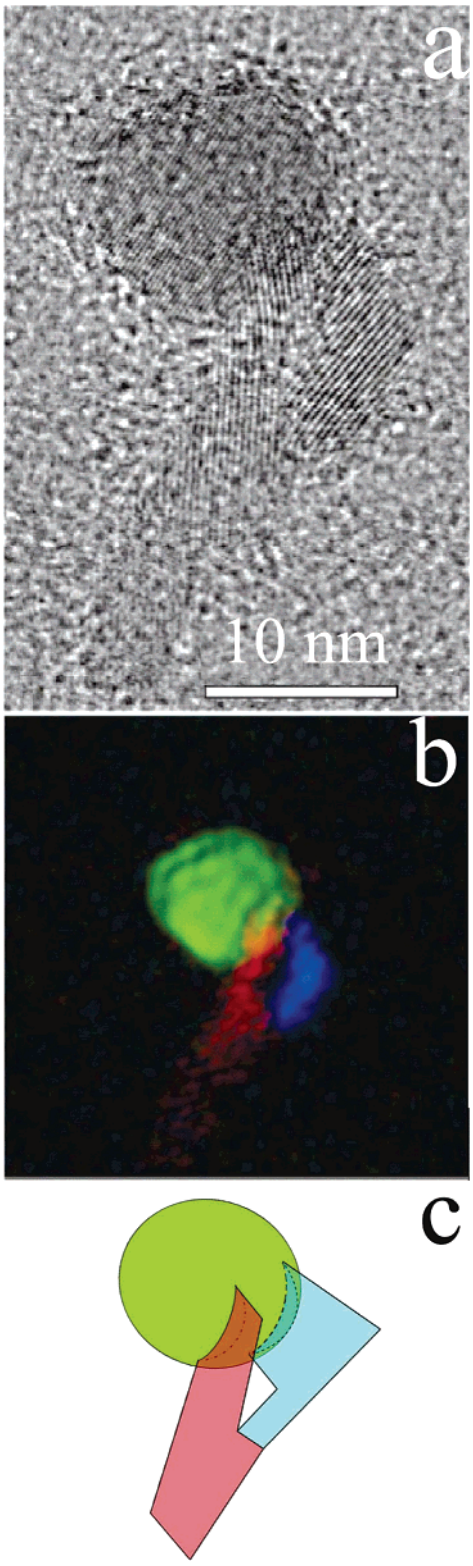

Figure 12. (a) HRTEM image of a branched TiO_2 NR that is attached to a maghemite sphere (in the ⟨102⟩ zone axis) by means of its two arms, in which only a set of fringes (namely the {011} and {01−1} fringes for the upper and the lower branch, respectively) are visible under this orientation. (b) False color map obtained from panel (a), revealing the domains of the two anatase arms (in red and blue, respectively) and the domain of the iron oxide sphere (in green). (c) Proposed structural model for the junction between the branched NR and the sphere.

between the sphere and each arm is locally confined to a rather small area of the sphere. In addition, the directions of the arms

depend on the local inclination of the plane tangent to the sphere. A possible scheme of the junction is proposed in panel c.

Besides the above-described geometries, heterostructures with the two oxide domains in a Ø-like configuration were observed in BNC population, although they occurred less abundantly. One example is shown in Figure 13. The nanorod appears to be surrounded by an iron oxide sphere, as demonstrated by the false color elaboration in the panel c. The shape of the border between the two domains proves that the two objects are actually intersecting. In spite of the different geometry, the zone axes as well as the relative orientation in which the particles are observed, are very similar to those reported in Figure 10. This can be considered as strong evidence that the relative positioning of the two lattice domains follows precise crystallographic relationships. The geometry of these latter heterostructures does not allow distinguishing the details of the rod/sphere interface. Nevertheless, from the observations reported above, the number of misfit dislocations can be reasonably expected to be higher with respect to the other BNC types, as the shared interface is much more extended.

4. Discussion

We have developed the colloidal synthesis of a novel type of hybrid BNC, comprising one rodlike anatase TiO_2 section and one nearly spherical iron oxide (mainly γ-Fe_2O_3) particle permanently attached together. The proposed synthetic strategy relies on seeding the growth of iron oxide with TiO_2 NRs by manipulating $Fe(CO)_5$ decomposition in a ternary surfactant mixture. This method is highly versatile in that it allows for the preparation of BNCs with domains of tunable dimensions by adjusting several reaction parameters. The topologically controlled composition of the BNCs was ascertained by combining ensemble characterization techniques, such as powder X-ray diffraction, Raman and Mössbauer spectroscopy, with detailed investigations of individual BNCs by HAADF imaging and HRTEM.

Mechanism of Heterostructure Formation. The formation of iron oxide NCs was observed at a minimum reaction temperature of ~220 °C, which lies above the decomposition point of $Fe(CO)_5$ (~170 °C).[39] This finding suggests that the active species leading to the production of iron oxide NCs (commonly referred to as the "monomers") are provided by thermal decomposition of the Fe−surfactant complexes present in the solution.[30,39] Within experimental error, XRD and HRTEM investigations proved that the BNC samples that were not exposed to air were already composed of a Fe_3O_4/γ-Fe_2O_3 mixture without metallic Fe. Therefore, it can be concluded that, under the employed reaction conditions, iron oxide is formed by direct pyrolysis of Fe/O-containing species during the high-temperature step under nitrogen,[30b,c] while the subsequent air treatment step ensures almost complete oxidation of the Fe_3O_4 phase into γ-Fe_2O_3, in agreement with our Mössbauer analysis.

The reactions of $Fe(CO)_5$ in hot surfactant mixtures have been widely studied.[30,39] In such systems, the supersaturation threshold is crossed after an induction period required for the accumulation of a sufficiently high concentration of monomers.[30b,c,f,39b] Differently, subsequent growth of the initially generated nuclei is comparatively much faster. It follows that a temporal separation between the nucleation and the growth stages is naturally achieved during iron oxide syntheses.[30,39b]

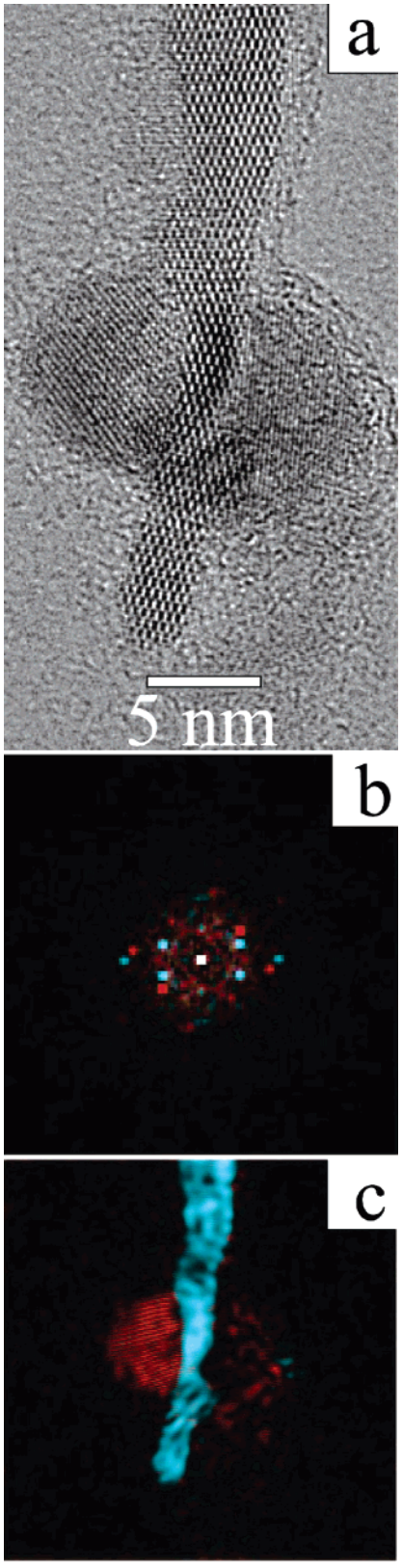

Figure 13. (a) HRTEM image of TiO_2 NR crossing the middle of a maghemite particle. (b) Merged diffractograms of the two phases: the respective zone axes are along the ⟨100⟩ direction of anatase and along the ⟨100⟩ direction of maghemite. (c) False color elaboration evidencing the relative positioning of the two particles. In panels b,c, red indicates the {02−2} fringes of iron oxide, and blue indicates the {01−1} fringes of anatase. The shape of the border between the two domains is a proof that the two objects are actually intersecting.

Therefore, by deliberate introduction of preformed NCs into the monomer solution it should be possible to trigger preferential growth onto such seeds (heterogeneous nucleation), while suppressing the generation of novel embryos (homogeneous nucleation) to a considerable extent. In the classical nucleation theory, an equivalent way of describing this mechanism is that the activation energy for homogeneous nucleation of NCs in solution is much higher than the barrier for heterogeneous growth on pre-existing nuclei.[51] The validity of this concept has been widely demonstrated in a variety of seed-mediated strategies for preparing larger NCs from smaller particles,[1,2,29a,c,g] as well as for creating core/shell NCs.[7−12]

The above concepts can be equally applied to rationalize the formation of the TiO_2/γ-Fe_2O_3 BNCs. In our colloidal system, TiO_2 NRs act as sites for the heterogeneous nucleation and growth of iron oxide domains. The observed time evolution of the BNC topology and dimensions strongly supports this mechanism. Indeed, the heterostructure formation proceeded via direct nucleation of iron oxide "patches" onto TiO_2, followed by the gradual enlargement of these domains over time. In contrast, any sort of particle-aggregation-based mechanism would involve the initial nucleation and growth of separate iron oxide NCs, which should subsequently attach to the TiO_2 NRs. In the latter hypothesis, one should detect the progressive increase in the population of BNCs at the expense of the population of both the NRs and of the already formed iron oxide spheres. However, such an evolution was never observed, whereas the relative fractions of the BNCs and isolated nanospheres kept nearly constant over time. As a further confirmation, the heating of mixtures of TiO_2 NRs and iron oxide NCs provided by separate syntheses never resulted in the permanently linked NR/sphere paired structures. In fact, the almost exclusive formation of binary rod/sphere NCs further discredits any fusion-based growth mechanisms, as the latter should in fact lead also to other types of particle aggregates, such as rod or sphere oligomers, and/or combinations of them. On the other hand, oriented attachment has thus far been observed to occur only among NCs of the same material.[52] Finally, the collected data allow one to exclude even a de-wetting process in the formation of the BNCs.[14] In the latter hypothesis, the transient formation of a thin shell around the NRs should be observed, followed by its coalescence into a single distinct domain upon a thermal annealing process. However, no proof in favor of such a growth sequence was found.

On the basis of all the above arguments, it can be additionally inferred that the iron oxide NCs which grow separately in the samples are the product of homogeneous nucleation. The mean size and size distributions of these NCs are close to those of the iron oxide domains in the BNCs, thus suggesting that the homogeneous and heterogeneous nucleation occur almost concomitantly in the system. However, the moderate size distributions attained highlight that nucleation is somewhat prolonged over time.

Control of the BNC Yield and of the Iron Oxide Domain Size. The results of our syntheses, such as the relative populations of the various particle types, the BNC yield, and the size control achieved for the maghemite domains, can be ultimately traced to the competition between homogeneous and heterogeneous nucleation events, and to the established balance between nucleation and growth stages. These processes are regulated by the combined effects of the reaction temperature and the relative $TiO_2/Fe(CO)_5$ concentration ratio, as follows.

The individual effects of temperature and iron precursor concentration were disclosed by syntheses carried out in highly concentrated TiO_2 solutions (>0.30 M), a condition selected to "saturate" the probability of heterogeneous growth. These experiments highlight that the BNC yield, which reflects the extent of heterogeneous nucleation, is governed mainly by temperature, whereas it is little affected by changes in the $Fe(CO)_5$ concentration. This can be understood within a simple microscopic mechanistic picture. For iron oxide to deposit onto TiO_2, it is required that the monomers first approach and then react with the seeds. Nevertheless, the TiO_2 NR surface accessibility is hindered by the presence of a passivating layer of organic stabilizers. Higher temperatures promote a faster exchange dynamics between the surfactants bound to the NR seed surface and the free ligands in the solution. Also, the diffusion rate of the monomers is expected to increase significantly. As a result, the average probability of heterogeneous nucleation should become higher. Such expectation actually agrees well with the temperature dependence of the heterostructure yield found experimentally in the 240−300 °C range. Moreover, at progressively higher reaction temperatures, a decrease in the mean iron oxide domain size of the BNCs is simultaneously observed for a fixed amount of $Fe(CO)_5$ injected. This finding can be understood by considering that, once iron oxide patches are deposited, subsequent monomer reaction proceeds preferentially at such pre-existing sites. Consequently, the greater the number of iron oxide domains that are generated is, the lower is the monomer concentration left to feed the initially formed domains, which will therefore grow only to comparatively smaller dimensions.[18a]

The fraction of the separately grown iron oxide NCs, which reflects the degree of homogeneous nucleation, is influenced by both the temperature and iron precursor concentration. At a fixed $Fe(CO)_5$ content, increasingly high reaction temperatures lead to only minor increments in the population of these NCs. Indeed, the large depletion of monomers in the heterogeneous nucleation can quickly reduce their concentration below the supersaturation threshold.[51] Differently, when progressively higher $Fe(CO)_5$ amounts are used (>0.15 M) at a fixed temperature, relatively larger iron oxide domains are obtained; however, the population of the isolated iron oxide NCs increases remarkably. Under such circumstances, the degree of heterogeneous nucleation remains nearly constant as it is indeed dictated by the temperature. It follows that the excess monomers cannot be quickly depleted below the supersaturation limit, and therefore additional homogeneous nucleation takes place.

Taken together, the above observations suggest that combining relatively high reaction temperature (∼270 °C) with low iron precursor concentration (∼0.05 M) can be a straightforward

(51) (a) Mullin, J. W. *Crystallization*, 3rd ed; Butterworth-Heinemann: Oxford, 1997. (b) Sugimoto, T. *Monodisperse Particles*; Elsevier: Amsterdam, 2001. (c) Markov, I. V. *Crystal Growth for Beginners: Fundamentals of Nucleation, Crystal Growth, and Epitaxy*; World Scientific: Singapore, 2003.

(52) (a) Tang, Z. Y.; Kotov, N. A.; Giersig, M. *Science* **2002**, *297*, 237. (b) Pacholski, C.; Kornowski, A.; Weller, H. *Angew. Chem., Int. Ed.* **2002**, *41*, 1188. (c) Cho, K. S.; Talapin, D. V.; Gaschler, W.; Murray, C. B. *J. Am. Chem. Soc.* **2005**, *127*, 7140. (d) Yu, J. H.; Joo, J.; Park, H. M. S.; Baik, I.; Kim, Y. W.; Kim, S. C.; Hyeon, T. *J. Am. Chem. Soc.* **2005**, *127*, 5662. (e) Zitoun, D.; Pinna, N.; Frolet, N.; Belin, C. *J. Am. Chem. Soc.* **2005**, *127*, 15034.

strategy to maximize the BNC yield, while minimizing the generation of separated iron oxide NCs. Under such conditions, the adjustment of the concentration of the TiO_2 NR seeds is a convenient tool to achieve controlled modulation over the mean iron oxide domain size. Indeed, when homogeneous nucleation is kept negligible, the TiO_2 concentration dictates the number of sites available for iron oxide deposition, thus regulating the ultimate balance of monomer consumption between the heterogeneous nucleation and growth stages. Hence, it appears clear that the lower the NR seed content is, the larger the iron oxide domain size will grow, according to the mechanisms discussed above.

Role of the Surfactants. A diluted ternary surfactant mixture was found to be a suitable growing medium for the BNCs. At present, it is difficult to decouple the detailed role played by each ligand species in the syntheses. Such a complication arises from the fact that the best results were obtained only when the three surfactants were simultaneously present in the reaction mixture, which implies that they behave synergistically. Oleic acid (OLAC), which binds strongly to TiO_2 surfaces, ensures the colloidal stabilization of the NRs, preventing them from aggregating and precipitating at high temperature. However, as OLAC also causes serious NR shrinking upon prolonged heating, oleyl amine (OLAM) is required as a competing surfactant to compensate for such OLAC-induced detrimental dissolution. As concerns the iron oxide-related chemistry, both OLAC and OLAM form complexes with the $Fe(CO)_5$ precursor, which feed the growing iron oxide NCs, as described above. Simultaneously, OLAC and OLAM are known as well to act as good colloidal stabilizers for iron oxide NCs. The presence of 1,2-dodecandiol (DDIOL), commonly employed as high-temperature reductant in many NC syntheses,[1,2] appears critical to guarantee high BNC yields. Since a zero-valence iron precursor is used, any DDIOL reductive action should be irrelevant. Therefore, it can be presumed that DDIOL modulates the dynamics of ligand adsorption/desorption on the TiO_2 NRs by competing with OLAC and OLAM. This participation may render the TiO_2 surface more accessible and therefore more reactive toward the monomers.

Origin of the BNC Topology. From the structural point of view, the most striking feature of the present BNCs is that the γ-Fe_2O_3 domain grows preferentially on the longitudinal sides (i.e., those parallel to the rod axis) of the TiO_2 sections. These TiO_2/γ-Fe_2O_3 asymmetric heterostructures are therefore remarkably different from the other hybrid NCs based on wurtzite CdSe, CdS, or ZnO rodlike seeds, that have been developed so far.[20−23] In the latter cases, the nucleation of the second material was, in fact, observed to occur almost exclusively on the rod tips, leading to matchstick- or dumbbell-like NCs.[20−23] Such specificity has been rationalized in relation to the inherent growth mechanism of the rod-shaped NCs. Upon facet-selective adhesion of suitable surfactants, materials that crystallize in phases possessing a unique axis of high symmetry (such as the wurtzite lattice) can preferentially expand either in the direction parallel or in the one perpendicular to such axis.[1,2,6] The less developed surfaces, i.e., the rod basal terminations correspond to the facets with the highest growth rate, as they are less efficiently passivated by the organic ligands. These facets are therefore more chemically accessible than the others, and a second material can be thus grown exclusively on these locations.

Analogously, the *c*-axis elongated tetragonal anatase TiO_2 seeds used in this work result from OLAC/OLAM-assisted anisotropic growth.[33,38] During the BNC synthesis, the TiO_2 {001} basal sides could be expected to be the preferred sites for iron oxide nucleation, as guaranteed by the surface-selective binding of the employed surfactants. Nevertheless, iron-oxide-tipped TiO_2 NRs were never formed. Neither TiO_2@maghemite core@shell NRs were observed. Therefore, it can be concluded that the growth mode adopted by iron oxide on the TiO_2 NR substrates should be dominantly driven by the high interfacial energy between the two materials,[53,54] rather than by the intrinsic chemical reactivity of the seed facets. Accordingly, the iron oxide domain will ultimately localize on the TiO_2 facet that minimizes the interfacial strain.

Interface Structure. The above suggested mechanism for the BNC formation is consistent with the peculiar structure observed for the interface between the TiO_2 and γ-Fe_2O_3 lattices, which indeed deserves further remarks. Detailed HRTEM and fringe periodicity analyses have revealed that the TiO_2/γ-Fe_2O_3 heterojunction does not develop in a straightforward way. The two domains share only a rather limited area, where the interfacial planes, identified as the {040} of maghemite and the {040} of anatase (parallel to the rod axis) in most cases, are deformed to match with each other. In contrast to what is observed for the isolated NRs, the TiO_2 section in most heterostructures appears distorted and slightly bowed toward the γ-Fe_2O_3 sphere to follow its curvature. This fact provides a clear evidence for the existence of a true inorganic junction between the two lattices, as such a linkage actually affects the structure of the individual material components. The coherent attachment of the two domains through a restricted and locally curved interfacial region appears to be the privileged bonding mode by which BNCs in various configurations can be indeed formed as, for instance, branched NRs attached to a γ-Fe_2O_3 particle by means of their arms.

The observed interface curvature at the TiO_2/γ-Fe_2O_3 junction can be explained as arising to accommodate locally the lattice strain and thus to allow iron oxide to grow coherently onto the TiO_2 NRs. This occurrence closely resembles a mechanism by which strain is relieved during MBE (molecular beam epitaxy) growth of quantum dot islands (QDIs) on highly mismatched substrates.[53,54] It is indeed established that the total energy in a volume of a strained material layer is given by the sum of the surface energy and of the strain energy.[53c,d] The latter contribution is directly related to the lattice misfit and can be decreased by a curling of the interfacial planes. This has been actually demonstrated by the possibility to grow nearly defect-free QDIs through local elastic deformation of the near-surface planes of

(53) (a) Kasper, E. In *Physics and Applications of Quantum Wells and Superlattices*; Mendez, E. E., von Klitzing, K., Eds.; Plenum Press: New York and London, 1987. (b) Le, Goues, F. K.; Copel, M.; Tromp, R. M. *Phys. Rev. B* **1990**, *42*, 11690. (c) Snyder, C. W.; Orr, B. G.; Kessler, D.; Sander, L. M. *Phys. Rev. Lett.* **1991**, *66*, 3032. (d) Snyder, C. W.; Mansfield, J. M.; Orr, B. G. *Phys. Rev. B* **1992**, *46*, 9551. (e) Pidduck, A. J.; Robbins, D. J.; Cullis, A. G.; Leong, W. Y.; Pitt, A. M. *Thin Solid Films* **1992**, *222*, 78.

(54) (a) People, R.; Bean, J. C. *Appl. Phys. Lett.* **1985**, *47*, 322. (b) Eaglesham, D. J.; Cerullo, M. *Phys. Rev. Lett.* **1990**, *64*, 1943. (c) Carlino, E.; Giannini, C.; Gerardi, L.; Tapfer, K. A.; Mäder, H.; von Känel, *J. Appl. Phys.* **1996**, *79*, 1441 and references therein.

both the substrate and the QDIs, which ultimately results in a wavy curved interface.[54]

The above mechanism is well suited to describe the nature of the interface in the present BNC heterostructures. Indeed, as the area shared by the TiO_2 and γ-Fe_2O_3 domains is rather limited and the interfacial planes are locally bent, the strain accumulated at the interface can be accommodated to a great extent, paying only a proportionally smaller cost of additional surface energy.[54c] By this way, the nucleation of dislocations can be considerably retarded even in the presence of a large misfit (e.g., for an interface close to a {040} plane of maghemite and the {040} of anatase, the mismatch is as high as ~8% and ~11%, in the directions perpendicular and parallel to the rod axis, respectively). Depending on the efficiency of strain relaxation, a coherently grown maghemite domain may actually have a higher stability than a dislocated domain because of the significant energy amount required to form dislocations.[53c,54c] Moreover, the interfacial strain ultimately dictates the lateral dimensions of the interface in the BNCs, in the same way as it does for the lateral size of QDIs.[53,54] Indeed, the realization of a rather extended junction area is an energetically disfavored event, because a high number of dislocations must be formed to relieve the elevate interfacial strain. This explains why the population of Ø-shaped BNCs with intersecting anatase−maghemite domains was smaller than that of other BNC configurations, which in fact shared a more limited interface with eventually just very few dislocations. In addition, when they are formed, dislocations should be spatially confined at the edges of the interface where the nonuniform strain field induced by the curved interface is indeed higher.[54c] This is again in perfect agreement with our HRTEM observations.

On average, only a single iron oxide domain is formed on each TiO_2 NR, regardless of the seed dimensions. This result is somehow surprising, as the probability of multiple heterogeneous nucleation can be expected to scale up the NR diameter and length, especially at high $Fe(CO)_5$ concentration, as larger seeds can offer more extended facets. It can be reasonably assumed that iron oxide patches will nucleate on those regions of the TiO_2 lateral facets where the surfactant binding is weaker or local surface crystal defects act as catalytic centers.[16] This would also explain why the relative positions of the two domains are not correlated by any special relationship. Once one iron oxide domain has formed on a TiO_2 NR facet, a polarization charge at the interface between the two materials can be induced. Owing to the higher average electron density of iron oxide, the other TiO_2 facets become enriched with electrons. Simultaneously, long-range strain fields can be induced in the heterostructure as a consequence of the interface bending. Both effects could be responsible for the inhibition of additional nucleation events.[15]

To conclude, our findings overall include novel structural observations as compared to those previously reported for other colloidal hybrid NCs, in which either a nearly flat junction area[14,15,18] or an interface developing through several couples of facets[20−23] have been identified. To the best of our knowledge, this is the first example of colloidal nanoheterostructures that are formed through a strain-driven heteroepitaxial growth mechanism based on a local bending of the interfacial planes.

Magnetic Properties. Finally, another remarkable result of this study is that the intimate junction with TiO_2 does not alter the characteristic size-dependent behavior of γ-Fe_2O_3, as highlighted by complementary Mössbauer and ac susceptibility measurements. Indeed, as the two domains communicate through a small contact area, the spin canting at the interface and the exchange coupling among the maghemite domains is not expected to be affected significantly,[15,18] differently from what is observed in core/shell systems.[7e−g,8−10,19a] This can be considered an advantage, in that the magnetic response of the BNCs will remain similar to that of isolated γ-Fe_2O_3 NCs, hence almost independent of the TiO_2 presence, and in turn, easily modifiable by controlling the maghemite domain size.

5. Conclusions and Perspectives

A seeded colloidal technique has been developed to synthesize a new type of asymmetric oxide BNCs with domains of tuneable size. Detailed compositional and structural data have been provided to demonstrate that each hybrid nanostructure is composed of one γ-Fe_2O_3 spherical particle coherently grown on a longitudinal facet of a semiconductor TiO_2 nanorod. The heteroepitaxial growth mechanism of the BNCs proceeds through the formation of a small curved interface as a means to accommodate the high interfacial lattice strain between the two material domains, which has been never reported before for colloidal heterostructures.

We believe that these TiO_2/γ-Fe_2O_3 BNCs will give rise to interesting advances in nanoscience. First of all, they could be used as model systems for investigating epitaxial relationships and topology evolution of hybrid NC systems as a function of interfacial strain. Such study may suggest useful criteria to engineer novel heterostructure geometries.

Second, the BNCs could serve to disparate technological applications. Indeed, these objects represent nanosized bifunctional catalysts for a variety of gas- and liquid-phase reactions. An especially appealing aspect of the heterostructures is that the photocatalytic activity of TiO_2 NRs is naturally combined with the magnetism of γ-Fe_2O_3. Once dispersed in homogeneous liquids, the BNCs could be efficiently fluidized and produce local heating of the solution upon application of an external magnetic field. Both effects could lead to more efficient light-assisted environmental remediation, after which the hybrid photocatalysts could be magnetically recovered for recycling.[24] Simultaneously, these BNCs offer the unique opportunity to study the effects of a local magnetic field on the photocatalytic performances of TiO_2,[55] as well as the influence of photoexcited TiO_2 charge carriers on the magnetic properties of the γ-Fe_2O_3 domain.

The BNCs could find exciting applications also in the biomedical field. The γ-Fe_2O_3 domain could be used to drive the BNCs toward tumoral tissues, where magnetically induced hyperthermia[32d−i] could be combined with TiO_2-based photodynamic therapy[28d−h] to kill malignant cells.

Finally, it could be possible to deliberately orient nanorods anchored on suitably functionalized and/or patterned surfaces under an external field. This would open up novel perspectives in the controlled assembly of multifunctional nanocrystals onto substrates.

Acknowledgment. This work has been partially supported by the EC-funded Novopoly STREP Project of the sixth EU

(55) (a) Zhang, W.; Wang, X.; Fu, X. *Chem. Commun.* **2003**, 2196. (b) Wakasa, M.; Suda, S.; Hayashi, H.; Ishii, N.; Okano, M. *J. Phys. Chem. B* **2004**, *108*, 11882.

FP (Contract No. STRP 013619) and by the Italian FIRB Contract No. RBLA03ER38. We are grateful to Dr. Tiziana Siciliano and Dr. Alessandra Genga (Dipartimento di Scienza dei Materiali, University of Lecce, Italy) for performing the Raman measurements, and to Dr. Liberato Manna (CNR-NNL, Lecce, Italy) for many inspiring discussions.

Supporting Information Available: HRTEM characterization of TiO_2 nanorods; TEM images of BNCs grown from larger TiO_2 seeds; TEM images of iron oxide NCs synthesized without TiO_2; Raman characterization of TiO_2 NRs and iron oxide NCs; magnetic measurements of BNCs in chloroform solution; Mössbauer characterization of bulk iron oxide materials and of iron oxide NCs synthesized without TiO_2; details on the Mössbauer fitting procedure; extraction of magnetic parameters from the Mössbauer data. This material is available free of charge via the Internet at http://pubs.acs.org.

JA066557H